**TURGUT ÖZAL UNIVERSITY**

**GRADUATE SCHOOL OF SCIENCE AND ENGINEERING**

**DEPARTMENT OF ELECTRICAL AND COMPUTER ENGINEERING**

# ASSESSMENT OF SPECIFIC ABSORPTION RATE AND TEMPERATURE INCREASE FOR ANATOMIC SHEEP MODELS DUE TO 3 TESLA MRI BODY COILS

**A MASTER THESIS**

**By**

**Hamza ERGÜDER**

**Supervisor**

**Asst. Prof. Tahir MALAS**

**Ankara, August 2015**

**TURGUT ÖZAL UNIVERSITY**

**GRADUATE SCHOOL OF SCIENCE AND ENGINEERING**

**DEPARTMENT OF ELECTRICAL AND COMPUTER ENGINEERING**

# ASSESSMENT OF SPECIFIC ABSORPTION RATE AND TEMPERATURE INCREASE FOR ANATOMIC SHEEP MODELS DUE TO 3 TESLA MRI BODY COILS

**A MASTER THESIS**

**By**

**Hamza ERGÜDER**

**Supervisor**

**Asst. Prof. Tahir MALAS**

**Ankara, August 2015**

**Statement of Scientific Ethics**

This thesis is prepared in accordance with the rules of Turgut Özal University Graduate School of Science and Engineering. I declare that:

- All information and documents within this thesis have been achieved in accordance wıth the academic rules.
- All visual, auditory, and written data and results are presented in accordance with the rules of scientific ethics.
- When used, other people's studies have been cited in accordance with the scientific standards.
- All studies that are cited are referenced properly,
- No fraudulent alterations have been done in used data.
- No part of this thesis has not been submitted as a thesis work neither in this university nor in another one.

.../.../…

**Hamza ERGÜDER**

## APPROVAL

Prepared by Hamza Ergüder, this work entitled "**Assessment of Specific Absorption Rate and Temperature Increase for Anatomic Sheep Models due to 3 Tesla MRI Body Coils**" has been found to be fully adequate, in scope and in quality, as a thesis for the degree Master of Science in Electrical and Computer Engineering Graduate Program of Graduate School of Science and Engineering by unanimous vote of the jury after the thesis defense on August 13, 2015.

**…….**

**Asst. Prof. Tahir MALAS (Chairman)**

**…….**

**Assoc. Prof. Özgür ERGÜL**

**…….**

**Asst. Prof. Ferhat Türker ÇELEPÇİKAY**

## ACKNOWLEDGEMENTS

This thesis could not have been written without Asst. Prof. Tahir Malas, who encouraged me through my whole academic program. I would like to thank him for giving me this opportunity and for his support, guidance and patience throughout the preparation and execution of this research.

I would like to thank to Assoc. Prof. Çağdaş Oto, Devashish Shrivastava, Samat Turdumamatov, Muhammed Ergül, Sümeyye Türker and Ceylin Gamze Sünger who supported and helped me throughout my research to complete. Without them, this thesis would not have been completed.

I would like also to thank to my lecturers, colleagues and all members of Turgut Özal University for their valuable help and friendship.

Most especially I would like to express my gratitude to my mother, father, brothers, grandmother, all of my family and all my friends who provide me to get everything that I have today, for their support, encouragement and love.

## ABSTRACT

**ERGÜDER, Hamza. Assessment of Specific Absorption Rate and Temperature Increase for Anatomic Sheep Models due to 3 Tesla MRI Body Coils, Master's Thesis, Ankara, August 2015.**

There is an increasing public concern about hazardous heating effects of radio-frequency (RF) coils used in high-field (≥ 3 Tesla) magnetic resonance imaging (MRI). To ensure RF safety, the power delivered to patients is regulated by setting limits on the whole-body specific absorption rate (SAR) and local SAR. For example, whole-body average SAR is limited to 2 W/kg for volume coils in normal mode of operation and it is limited to 4 W/kg for the first-level controlled mode that requires medical supervision. However, full-wave electromagnetic simulations of realistic anatomic models show that it is possible to significantly exceed the local SAR limits even if the whole-body SAR is kept below the specified limits that stated for 3T. It is interesting that such worrisome results of simulations are also obtained for 1.5 Tesla scanners that have been used for about 30 years with no known incidents of burning due to excessive heating.

To be able to explain such a dilemma, we consider computational analyses and in-vivo experiments with sheep. First, we constructed anatomic models of sheep with three levels of complexity from high-resolution computerized tomography images. Then, SAR results are obtained using the Sim4Life software, which uses the finite difference time domain method for electromagnetic calculations. Then, resulting temperature increase are obtained using two different bio-heat solvers. The first bio-heat solver is based on the classical Penne's bio-heat transfer model (BHTM). The second one is recently developed and is based on generalized bio-heat transfer model (GBTHM), which considers core-body heating that is ignored by BHTM. Indeed, our in-vivo experiments conducted in national magnetic resonance research center reveal that core-body temperatures do increase with a rate of 3 to 6 $^{o}$C per hour for a SAR level of approximately 2 W/kg. Hence, we observe that GBHTM results are reasonably close to experimental outcomes.

As a future work, we plan to elaborate on major error sources of both electromagnetic and bio-heat solvers and improve them. Then, we plan to repeat our computational analyses and in-vivo experiments on human body and explain the dilemma mentioned above.

**Keywords**

1. Bio-electromagnetics
2. Specific absorption rate
3. Bio-heat transfer model
4. Magnetic resonance imaging
5. MR Safety
6. Radio-frequency coils
7. Computerized tomography
8. Anatomic modeling
9. Finite difference time domain method
10. Method of moments
11. Finite element method

# ÖZET

**ERGÜDER, Hamza. 3T MRI Vücut Bobinleri İçerisinde Anatomik Koyun Modellerinin Özgül Soğurma Oranı ve Sıcaklık Artışlarının Değerlendirilmesi, Yüksek Lisans Tezi, Ankara, 2015.**

3 Tesla üzeri Manyetik Rezonans (MR) görüntülemelerde kullanılan radyo-frekansı (RF) bobinlerinin sıcaklık etkileri tartışılan bir konu haline geldi. RF güvenirliğinden emin olmak için hastaya göre belirli tüm vücut özgül soğurma oranı (SAR) ve lokal SAR değerleri bulunuyor. Örneğin, tüm vücut ortalama SAR normal durumda bir operasyonda 2 W/kg, gözetim altında birinci seviye kontrol durumunda 4 W/kg olarak limitlenmiştir. Ancak, gerçekçi anatomik modellerle yapılan tam dalga elektromanyetik simülasyonlar, tüm vücut SAR değerleri korunsa dahi lokal SAR değerlerinin yüksek oranda aşıldığını göstermektedir. 30 yıldır kullanılan 1,5 Tesla MR cihazları için yapılan simülasyonlarda da aynı endişe verici sonuçlar görünmektedir ancak bu ısınmaya karşı bilinen bir kaza olmamıştır.

Bu ikilemi koyun deneyleri ve simülasyonları yaparak açığa kavuşturmaya çalıştık. Öncelikle, yüksek çözünürlüklü bilgisayarlı tomografi görüntülerini kullanarak üç farklı seviyede anatomik koyun modeli oluşturduk. Ve elektromanyetik hesaplamalarda sonlu farklar zaman alanı yönetimini kullanan Sim4Life programı vasıtasıyla SAR sonuçları elde ettik. Sıcaklık sonuçlarını incelemek içinse iki farklı biyo-ısı çözücü kullandık. Bunlardan ilki, Penne'nin biyo-ısı transfer modelini (BHTM) temel olan bir çözücü idi. Diğeri ise BHTM'in vücut ısısı hesaplamalarına karşı yeni geliştirilen genelleştirilmiş biyoısı transfer modelini (GBHTM) temel alan bir çözücü idi. Ulusal manyetik rezonans araştırma merkezinde (UMRAM) yaptığımız koyun deneylerinde yaklaşık 2 W/kg SAR ile saatte 3 ile 6 °C sıcaklık artışı oldu ve buradan GBHTM sonuçlarının, deney sonuçlarına daha yakın çıktığını gözlemledik.

İlerdeki çalışmalarda, elektromanyetik ve biyo-ısı çözücülerin temel hatalarında daha özenli çalışarak, geliştirmeyi planlıyoruz. Simülasyon ve

deneylerimizi insan vücudunda da tekrar ederek bu ikilemi daha iyi açıklamaya çalışacağız.

**Anahtar Sözcükler**

1. Biyo-elektromanyetik
2. Özgül soğurma oranı
3. Biyo-ısı transfer modeli
4. Manyetik rezonans görüntüleme
5. Manyetik rezonans güvenliği
6. Radyo-frekans bobinleri
7. Bilgisayarlı tomografi
8. Anatomik modelleme
9. Sonlu farklar zaman alanı yöntemi
10. Momentler yöntemi
11. Sonlu elemanlar yöntemi

## Table of Contents

# ABBREVIATIONS

**2D** Two-dimensional

**3D** Three-dimensional

**BHTM** Bio-heat transfer model

**CT** Computerized tomography

**DICOM** Digital Imaging and Communications in Medicine

**FDTD** Finite difference time domain

**FEM** Finite element method

**GBHTM** Generalized **b**io-heat transfer model

**IEC** International electrotechnical commission

**MOM** Method of moments

**MRI** Magnetic resonance imaging

**RF** Radio-frequency

**SAR** Specific absorption rate

**T** Tesla

# TABLES

# FIGURES

# CHAPTER 1

## INTRODUCTION

For the last 30 years, magnetic resonance imaging (MRI) has been used successfully for diagnosis of illnesses. MRI produces higher-resolution images compared to other medical imaging modalities. In addition, thanks to recently developed 3 T and higher-field MRI systems, diagnoses of many neurological, metabolic and musculoskeletal system diseases have been possible.

During an MRI scan, in addition to the strong constant magnetic field, RF electromagnetic fields are transmitted to the region under interest to resonate water protons by MRI coils. This RF power causes temperature increase in tissues. Head, body, and extremity coils may cause heating on tissues because of exposure to the electromagnetic waves. Human experiments that have been performed approximately 30 years ago show that temperature increase is not in the dangerous level and concluded that MRI is a safe imaging technique. However, since the measurement of temperature increase on arbitrary locations is not practical, safety regulations are developed using specific absorption rate (SAR), which is related to RF power absorbed by the body.

In recent years, because of increasing interest to ultra-high-field MRI, which works at higher frequencies and requires higher power levels, there is again a concern regarding RF safety. Because of the danger and difficulty in making experiments with humans, researchers are motivated to make experiments with animals and perform simulations using computational techniques. Hence, there is an increase in the number of publications in this area. However, since results of animal experiments cannot be readily applied to humans and there is an inconsistency between the simulation and experiment results, the RF safety issue has not been clarified yet.

Because of the difficulties in estimating tissue heating, total source power delivered from RF coils are regulated by setting SAR limits. International Electrotechnic Commission (IEC) limits SAR as maximum of 2 W/kg for whole

body and 3.2 W/kg SAR for head. Those limits can be elevated to 4 W/kg for whole body under the first-level control mode. These limits allow power levels of up to 20-30 W for a head coil and 150 W for a body coil for an 80 kg adult male. We can realize that this power is much stronger compared to cellphones that radiate maximum 2W power. Moreover, due to SAR does not spread homogeneously inside the body, local SAR limits of 10 W/kg for body and head, and 20 W/kg for extremity are set by IEC to prevent local heating. IEC also recommends limiting temperature increase by 1 °C in the normal mode. For the first-level control mode, they suggest that core-body temperature should not exceed 40 °C. However, these limits are not controlled in practice.

First studies on MRI safety with human volunteers have been performed by Shellock et. al. [1]–[6]. They have some experiments on 35 patients with a head coil. The SAR levels are between 2.54 and 3.05 W/kg and they measure temperatures from skin, sublingual and cornea. They observe that only 0.5 °C increase occurs on the cornea. They also have same experiments with a body coil and conclude that temperature increases are very small; hence, they conclude that 1.5 T MRI scanners are safe for human.

In another study published in 1990, Barber et al. perform heating experiments with 12 sheep [7]. Unlike human experiments, they find significant increase in the blood and body temperatures. They also show that temperature increase scale linearly with both SAR levels and time. However, they do not use floroptic probes that are compatible with MRI scanners; hence the temperatures measured can be erroneous.

After those studies, very few publications arose related to MRI safety until the advent of ultra-high-field MRI. Recently, Devashish et al. preform some experiments with swine and show that local SAR limits can be significantly exceed even though whole-body SAR limits are followed [8]–[11]. He also show that there is a linear increase of core-body temperature when volume coils are used.

In this study, unlike to the previous ones, we try to validate simulation results with experiments. For this purpose, we first generate anatomic models of a sheep using Mimics software. This task is elaborated in Chapter 2. Then, we perform simulations with Sim4Life software using the developed sheep models and analyze

anatomic models with various complexities. We also compare two different bio-heat solvers. These simulations are explained in Chapter 3. Then, in Chapter 4, we present in-vivo sheep experiments. Finally, we conclude in Chapter 5 by comparing in-vivo experiments with simulation results and referring to some future work.

# CHAPTER 2

## CREATION OF ANATOMIC SHEEP MODELS

Creating an anatomic model is the first and major part of this work. The images to create a three-dimensional (3D) model can be obtained from computerized tomography (CT) or MRI. These images correspond to axial, sagittal, or coronal slices of the body of the patient, as shown in Figure 1. 3D models are constructed from those two-dimensional (2D) images. Depending on the number of slices and resolution of the images, the 3D model can have better quality and be more realistic.

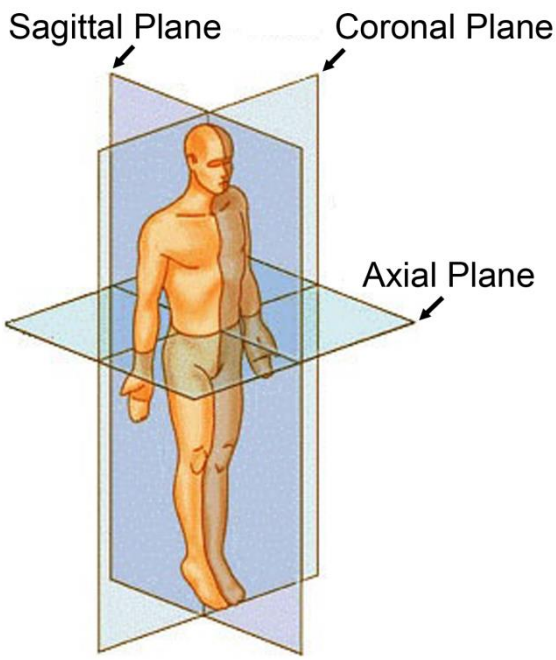


**Figure 1** Anatomic planes of the human body

Being one of the most widely used imaging modality to investigate the human anatomy; MRI has found many applications in medical diagnosis. Today, about 25,000 scanners are estimated to be in-use worldwide [12]. In many medical diagnosis and treatments, MRI is proven to be very effective [13].

In MRI, tissues and organs can be recognized more easily compared to older imaging modalities, such as CT [13]. For instance, unlike CT, one can distinguish white matter and gray matter in brain with MRI as shown in Figure 2. Due to this higher soft-tissue contrast, MRI allows us to create more detailed anatomic model than CT does [14], [15]. However, gray values of some tissues can be very fitful. In some slices those values become close to zero, and in some other slices they become close to the brightest value. At the same time, different tissues may have gray-scale values that are very close to each other. Hence, it becomes impossible to make use of the automatic functions provided by segmentation software to identify some tissues rapidly.

CT is a medical imaging modality that provides the interior view of the body with detector-taken X-rays from different angles. The word tomography consists of a combination of "tomos" and "graphia" which are from Greek. "Tomos" means slice and "graphia" means describing. CT was invented in 1972 by engineer Godfrey Hounsfield and by physicist Allan Cormack. First CT scanner took several hours to acquire the raw data and took days to reconstruct a single image from this raw data. Today, CT devices can collect four slices of data in about 0.3-0.4 second and reconstruct a 512 x 512-matrix image from millions of data points in less than a second. In Figure 3, we show two images obtained with CT to demonstrate the progress obtained with CT.

In CT images, some tissues, such as bone, can easily be recognized. For instance, CT shows bones much brighter compared to other tissues. Fat and muscle tissues can also be easily recognized. Although white and grey matters in brain or some other tissues cannot be distinguished as clear as in MRI, fairly accurate anatomic models that contain seven or eight tissues can be constructed using CT images. Since we consider heating due to volume coils and do not consider small loop coils or implants for which more detailed models can be necessary (see [15] for instance for a case study in which SAR results do change with anatomic details), models obtained from CT images has been satisfactory enough for our purposes.

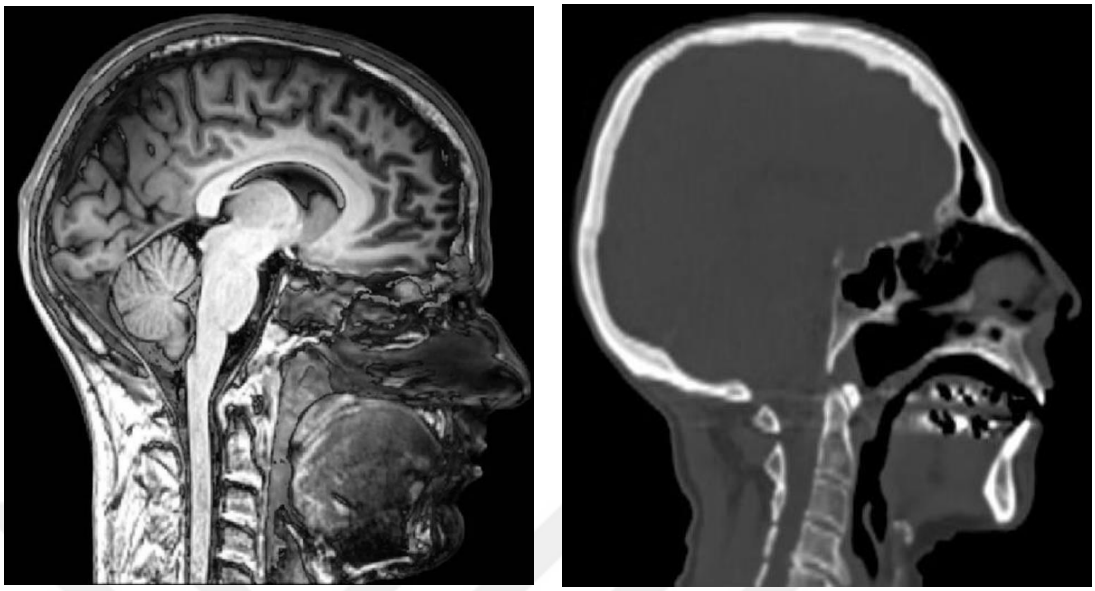

a) **A sagittal slice by MRI** b) **A sagittal slice by CT**

**Figure 2** A sagittal scan of brain which clearly shows the difference between MRI and CT images

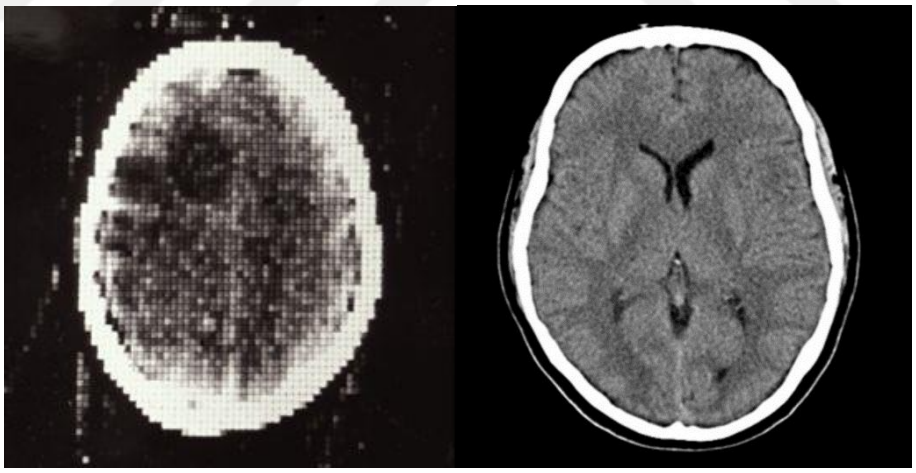

a) The first clinical scan performed in 1971 b) A brain scan, today.

**Figure 3** A comparison between early and modern CT images

## 2.1 Anatomic Modeling with Mimics

In this work, we used Mimics software to construct 3D anatomic models [16]. Mimics is an interactive application that facilitates 3D model creation from CT and MRI images using its built-in functions. The common format of CT and MRI images is DICOM (abbreviated from “digital imaging and communications in medicine”) which can easily be imported by Mimics. The process of 3D model construction is elaborated in Figure 4.

After importing DICOM images into Mimics, a screen comes in view with three different angles including axial, coronal and sagittal views (Figure 5). The tissues we want to mark should firstly be created as a mask in this section. Other tasks that should be followed are described below.

### 2.1.1 Segmentation

Segmentation is a marking operation that distinguishes tissues from CT and MRI images. We should choose tissues we recognize on the images with the threshold functions. Mimics has various segmentation functions. Threshold, region growing, Boolean operators, cavity fill, single and multiple slice edit, mask edit in 3D are the functions we use to segment the tissues.

#### 2.1.1.1 Threshold

All the pixels of images have a gray-scale value. Pixels that belong to the same tissue have generally gray values that are close to each other in CT images. Especially, the bone has distinctly different gray values from other tissues. In Figure 6, we depict the threshold values used for segmentation of bone. Threshold function delimits the gray values that marked to segment the images. Thus we easily segment the tissues.

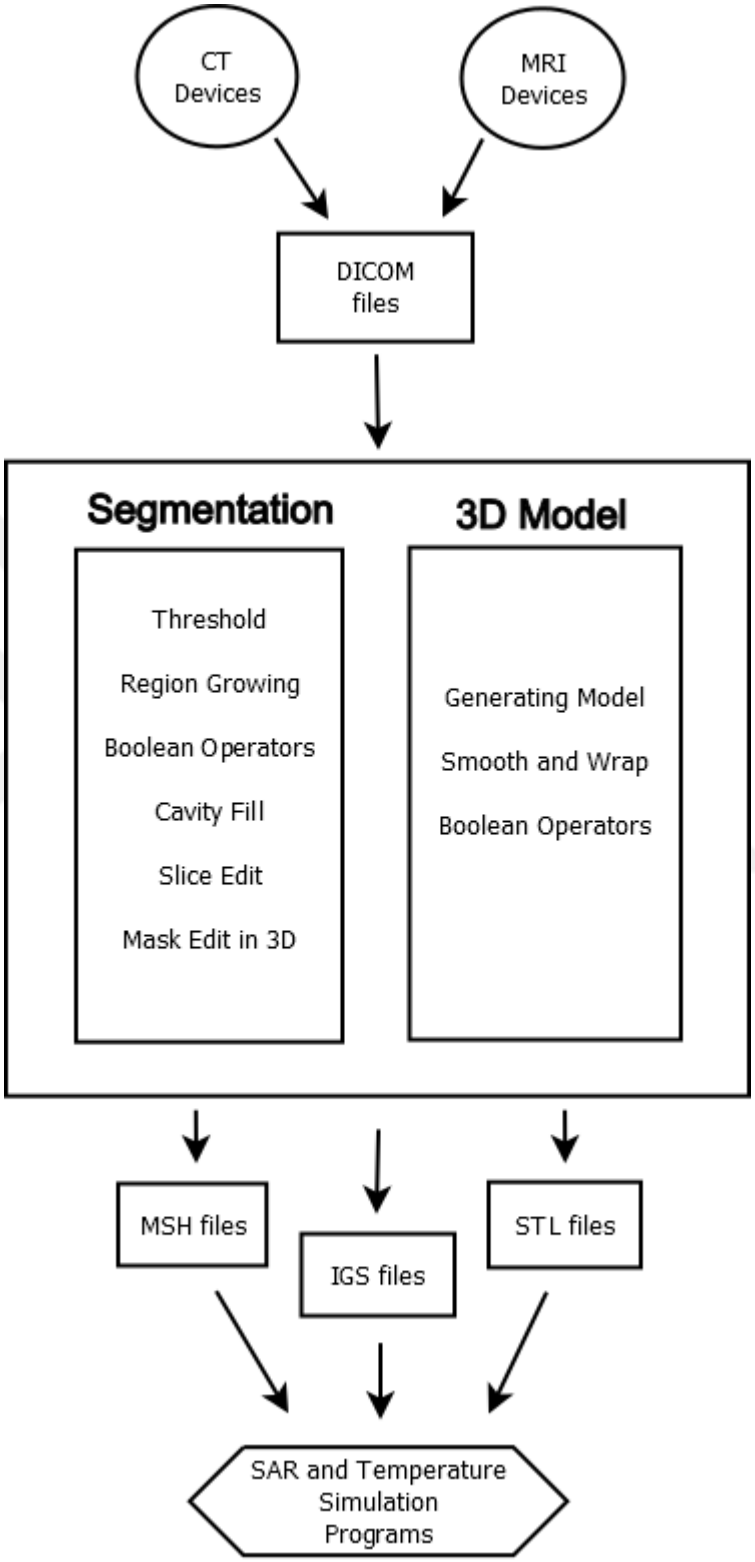


**Figure 4** Scheme of modelling process using Mimics software

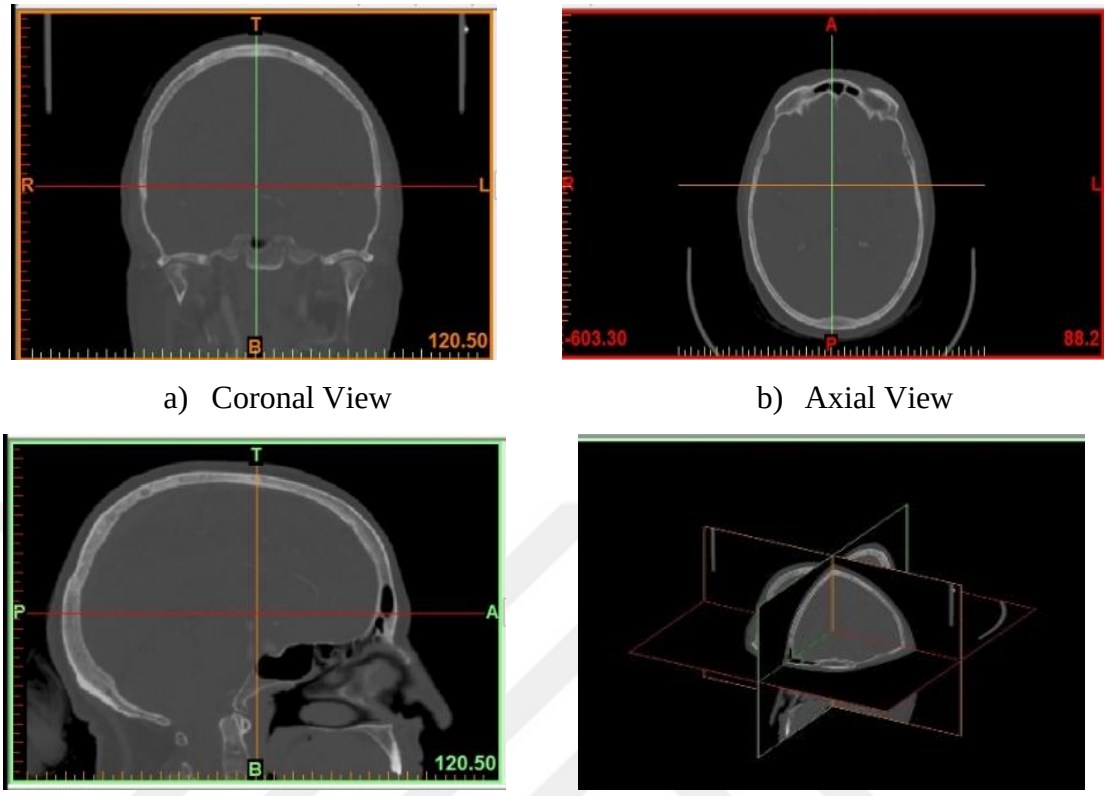


a) Coronal View b) Axial View

c) Sagittal View d) 3D View

**Figure 5** First view screen on MIMICS after creating a project

The threshold section comes in view after we create a mask for a tissue. There are max and min values to choose the range of pixels gray values as displayed in Figure 6. Tissues can be defined based on one value or based on min and max threshold value. The segmented tissue will contain the pixels in the images that have values between higher and lower threshold values. Figure 7 and Figure 8 shows Mimics screens before and after segmentation of the bone.

### 2.1.1.2 Region Growing

Region growing provides the capacity to split the segmentation into separate tissues. If we have a mask that ınclude more than one tissue, as shown in Figure 8, we can use region growing to create mask for each other. After selection of initial pixels, this function segments the neighboring pixels that have similar gray values to initial pixels. Thus, we can easily separate the tissues.

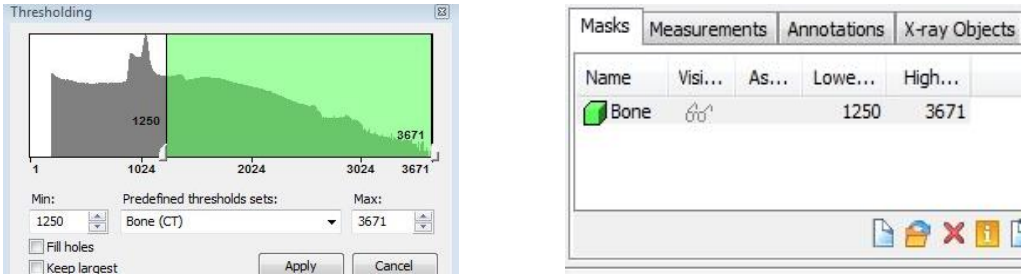


**a** **b**

**Figure 6** The threshold functıon of Mimics: a) Threshold screen b) Mask screen

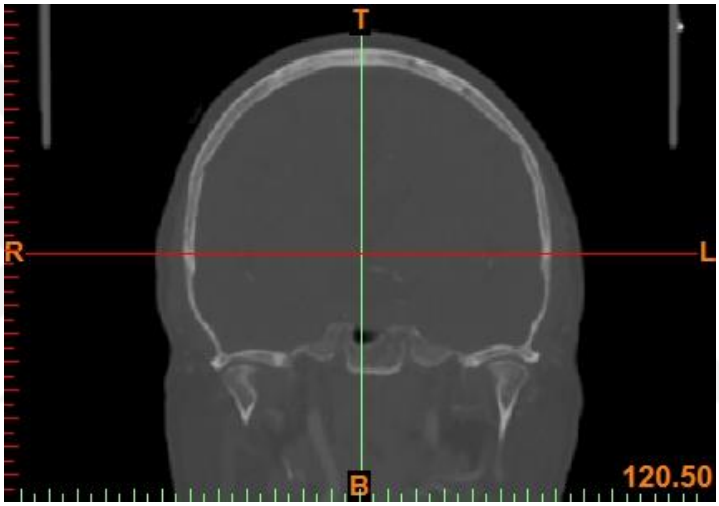


**Figure 7** The first view of imported CT images before segmentation

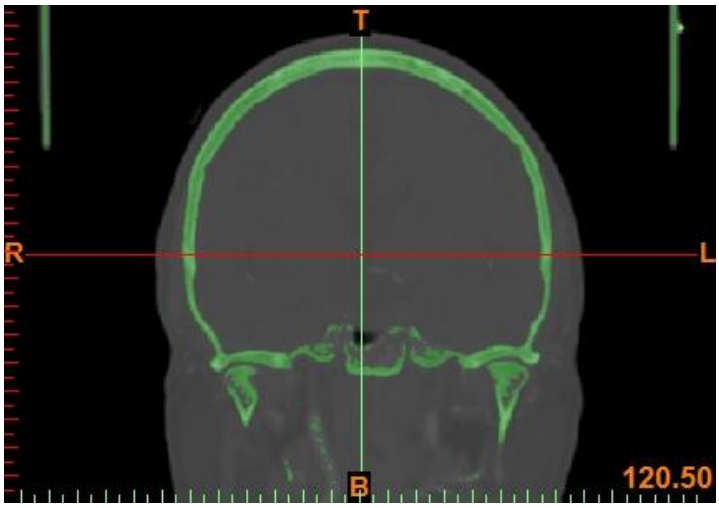


**Figure 8** A screen view of Mimics after applying a threshold


**Figure 9** Region growing screen

We can also segment with using dynamic region growing function. It is like region growing function, but this function allows us to segment a tissue based on the connectivity of gray values in a range. A threshold will be set based on min and max values nearby selected pixel. An example use of this feature is shown in Figure 10.

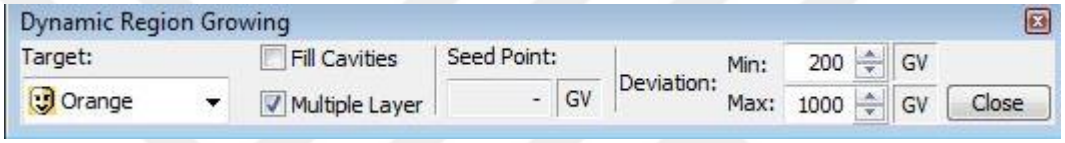


**Figure 10** Dynamic region growing screen

When using the region growing function, we can choose bone only as shown in Figure 11. Here, we separate bone from sticks on image's upper right and left sides.

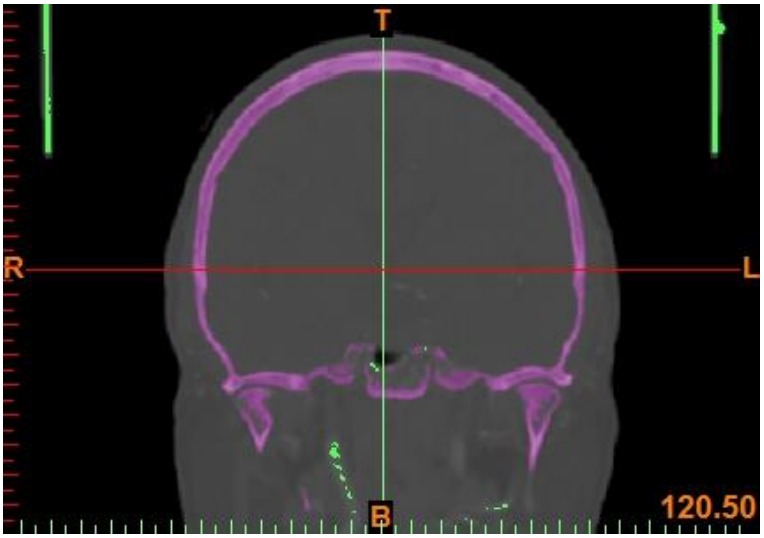


**Figure 11** Segmentation using region growing function from the threshold mask

### 2.1.1.3 Boolean Operators

These operators are used to create a new mask with union, intersection, or subtraction of two masks. Typical uses are to subtract a tissue from the whole body or unite masks that consist of the same tissue. An example of use is shown in Figure 12. Here, to classify all of the pixels, we first create a homogeneous model. Then, we subtract other tissues from homogeneous model. In this way, all pixels inside of human can be described.

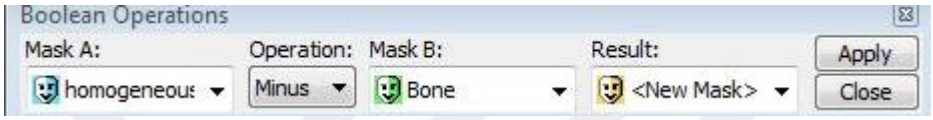


a) Boolean Operators screen

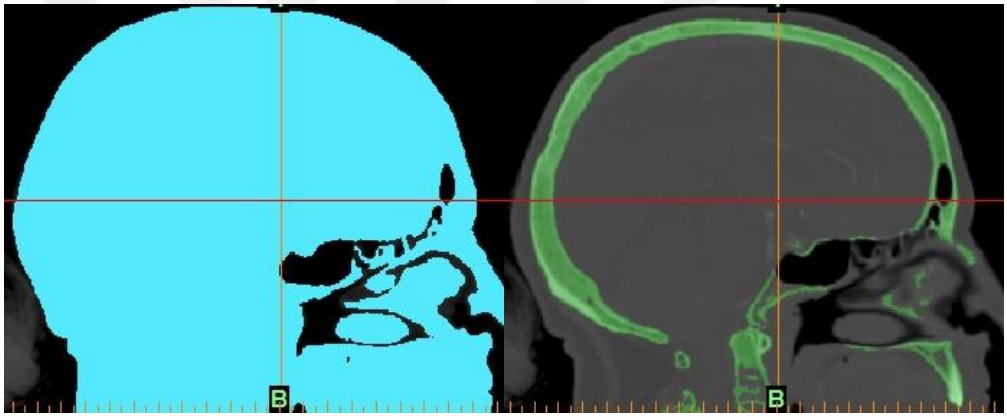

b) Segmented homogeneous model c) Segmented bone tissue

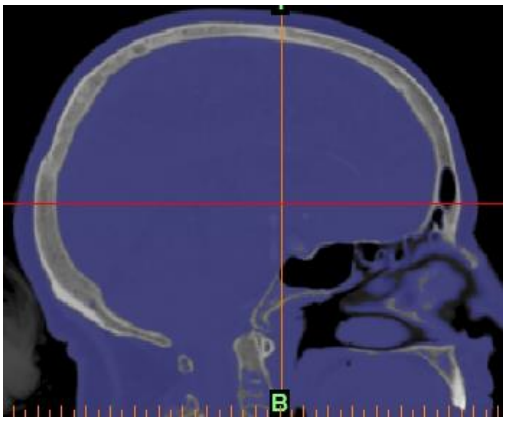

d) After subtraction operation with two masks in Figure 12-b and c

**Figure 12** Boolean Operators

#### 2.1.1.4 Cavity Fill

This function (Figure 13) can be used to fill interior of a mask that sets the boundaries. For instance, after skin tissue segmented, we can create a homogeneous model by filling inside of it using the cavity fill function. In Figure 14 we show how this feature can be used to mark empty (unmarked) region.

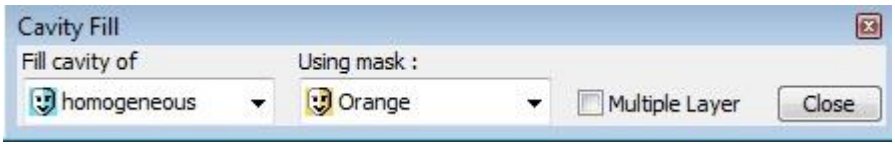


**Figure 13** Cavity fill screen

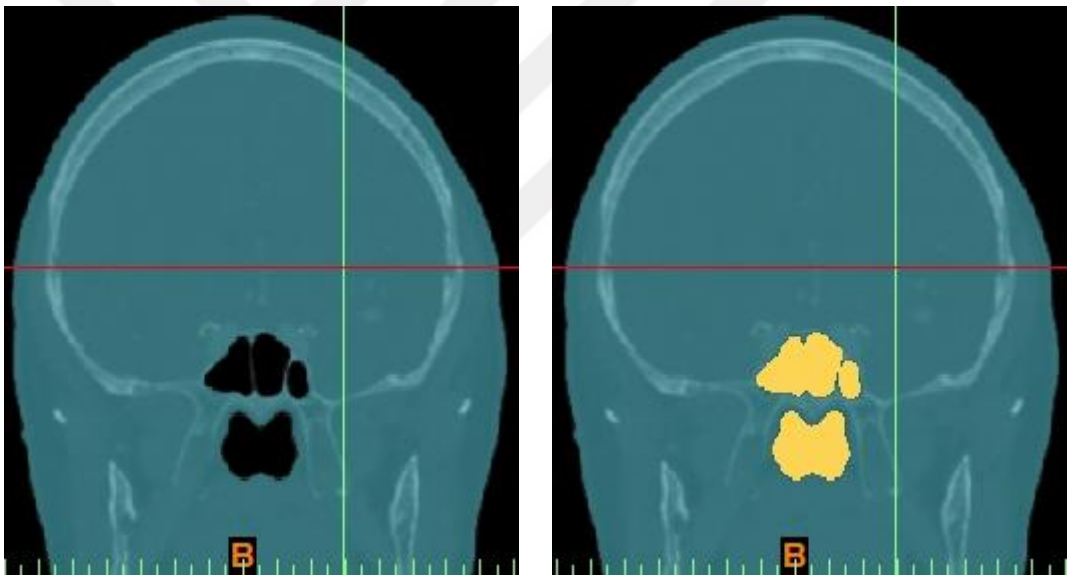

**Figure 14** Illustration of the cavity fill function: Left, before cavity fill; right after cavity fill is performed

#### 2.1.1.5 Single and Multiple Slice Edit

Any tissue that cannot be automatically segmented using the aforementioned techniques has to be segmented manually with these editing functions. Using slice edits, we can draw or erase regions on images. With the threshold feature of these functions, we can also ignore some pixels that have different gray values from the considered tissue.


**Figure 15** Multiple slice edit setting screen

More than one slice can be edited clearly using multiple slice edit, which works by creating temporary mask that can be edited. At the same time, it interpolates temporary masks between different slices with its extruding feature.

#### 2.1.1.6 Mask Edit in 3D

No matter how carefully we perform segmentation of slices, 3D visualization and evaluation of the final result is necessary. Mask edit in 3D removes and fixes some erroneous parts. In addition, if a mask has two different tissues or organs that we want to separate, the function lets us separate them as shown in Figure 16.

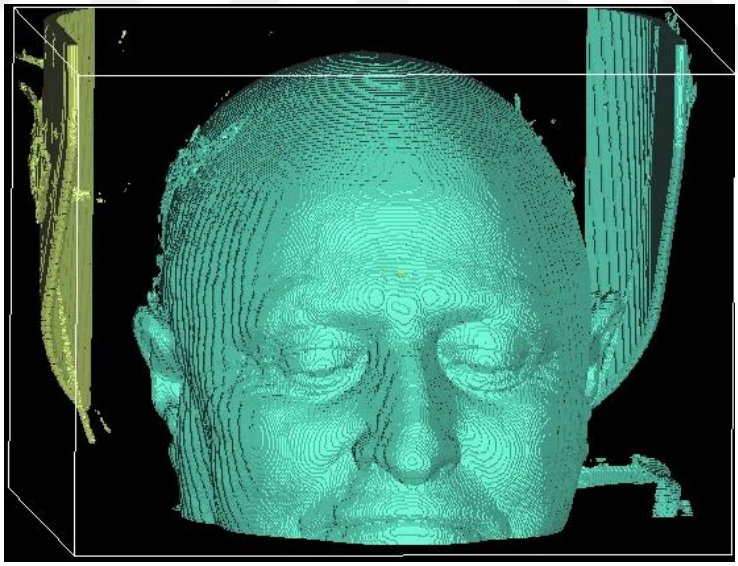

**Figure 16** Removing a wrong segmented part of a tissue with mask edit in 3D function

#### 2.1.1.7 Creation of the 3D Model

After segmentation of all tissues, a 3D model can be created in low, medium, or high qualities. For the low-quality mode, created voxels have bigger size. Hence,

the model may not be accurate enough and some details of anatomic regions can be lost. On the other side, the generation of high-quality models takes too much time and occupies a significant amount of memory. Hence, there is a trade-off that needs to be considered. As a rule of thumb, we require that basic anatomic features, such as fat thickness or bone shapes need to be preserved.

The created model may have some gaps and roughness. After generating 3D model, wrap and smooth functions can be used to fix those kinds of distortions. In Figure 17, we display accurate 3D model of bone that has been obtained after some iterations.

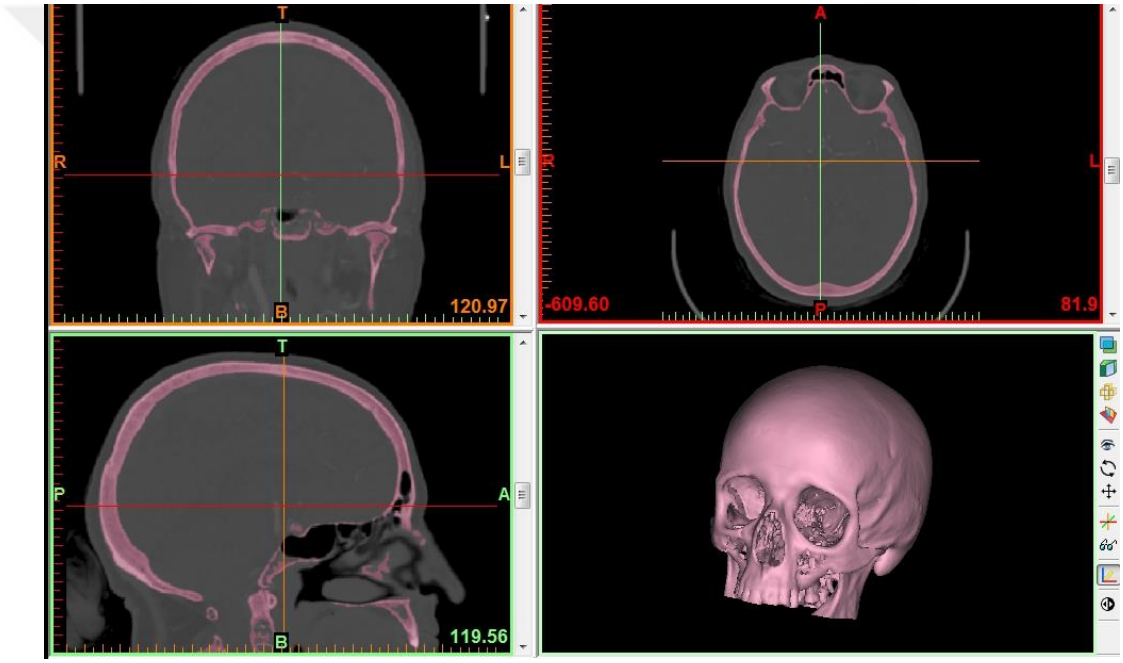


**Figure 17** Segmented bone tissue generated as a 3D model

## 2.2 Creation of 3D Sheep Models

### 2.2.1 The Head and Neck Model

Before deciding to use CT data, as a first try we started with the head and neck of a sheep which is prepared from MRI images. The resolution of the image-set obtained using T1 weighting is 1.56 mm x 1.56 mm x 1.56 mm. As we can see from Figure 18.a, in MRI many tissues can be recognized but they have close gray values.

First, we want to see the effects of complexity of the model on SAR distribution. For that purpose, we created homogeneous, three-layered, and anatomic models. The homogeneous model (Figure 18.b) has been assumed to consist of only muscle tissue, similar to phantoms used in evaluation of SAR experiments. The three-layered model has approximately 4-5 cm thick skin and fat layers, and muscle tissue inside (Figure 18.c). Finally, we segment six tissues for the anatomic model (Figure 18.d), which are brain, bone, fat, skin, muscle and internal air. To segment these tissues, instead of automatic segmentation, we generally have to use edit slice function of Mimics. The color bar that refers to tissues is shown in Figure 19.

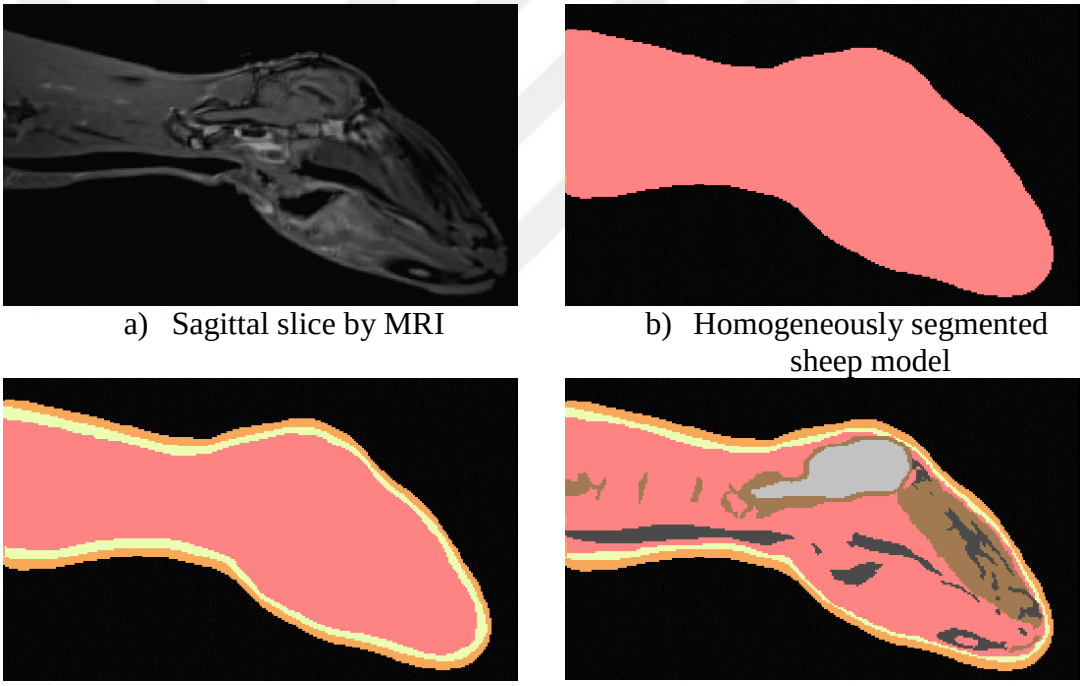

a) Sagittal slice by MRI

b) Homogeneously segmented sheep model

c) Three-layered segmented sheep model

d) Anatomicly segmented Sheep model

**Figure 18** Head and neck slice of the sheep


**Figure 19** Color map of tissues of the head and neck model

When all the tissues are segmented, we generate the 3D head and neck model. After some smoothing operations, the model is ready to export as shown in Figure 20.

**Figure 20** 3D head and neck sheep model

### 2.2.2 The Whole-Body Model

Next step of this project is creating a whole-body sheep model. For this purpose, we obtain new MRI and CT images. Resolutions of these images are sufficiently appropriate; 1.17 mm x 1.17 mm x 1.17 mm for MRI and 0.6 mm x 0.85 mm x 0.85 mm for CT. A sagittal slice of CT image is shown in Figure 21.

For the head and neck model, we used MRI images. We note that, when MRI is used, obtaining even a three-layered model requires more time and effort compared to obtaining models from CT images. Actually, it is stated that segmentation of a whole body using MRI data can easily exceed six person months [15]. Therefore, in whole- body modelling, we use CT images.

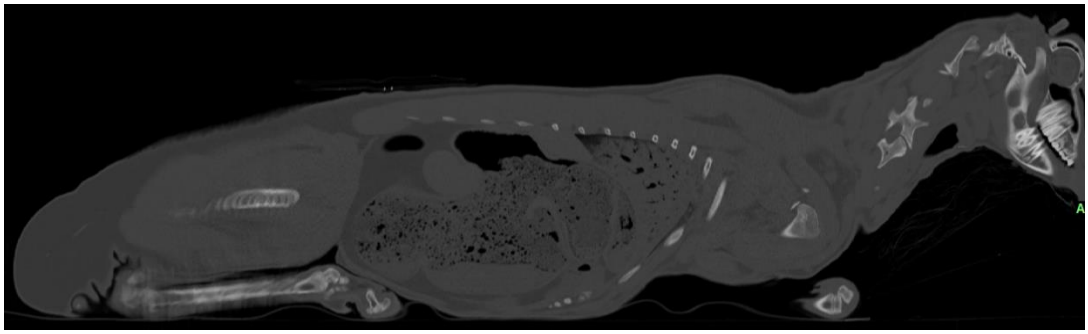

**Figure 21** A slice of a full body sheep imaged with CT

Similar to the head and neck models, for whole body, we create three models, namely, homogeneous, three-layered and seven-tissues anatomic models. We segment homogeneous model using threshold, region growing and cavity fill functions. As can be seen in Figure 22, we segment the sheep fully as just one muscle tissue. After segmentation of the homogeneous mask, we generate 3D model and use some smoothing and wraping functions to obtain final model shown in Figure 23.

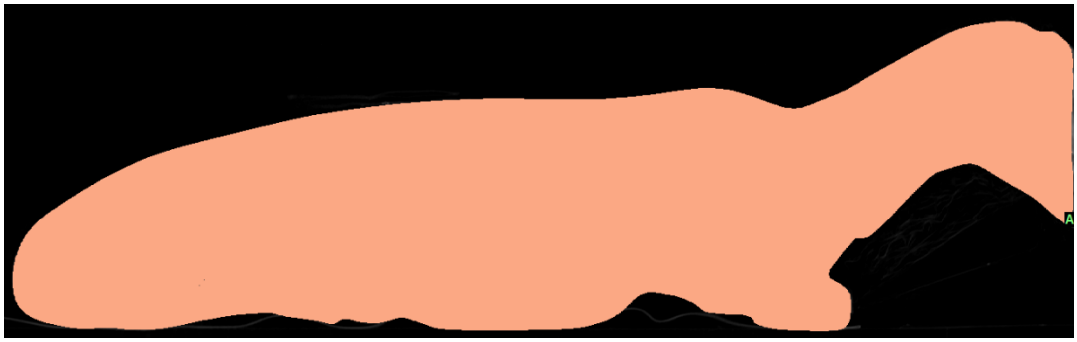

**Figure 22** A homogeneously segmented mask of a whole-body sheep

As in the head and neck model, the three-layered whole-body model consists of skin, mucscle, and fat tissues, as shown in Figure 24. After segmentation of three layered mask, we generate the 3D model. We utilize smoothing and wraping functions and finally obtain the model, shown in Figure 25.

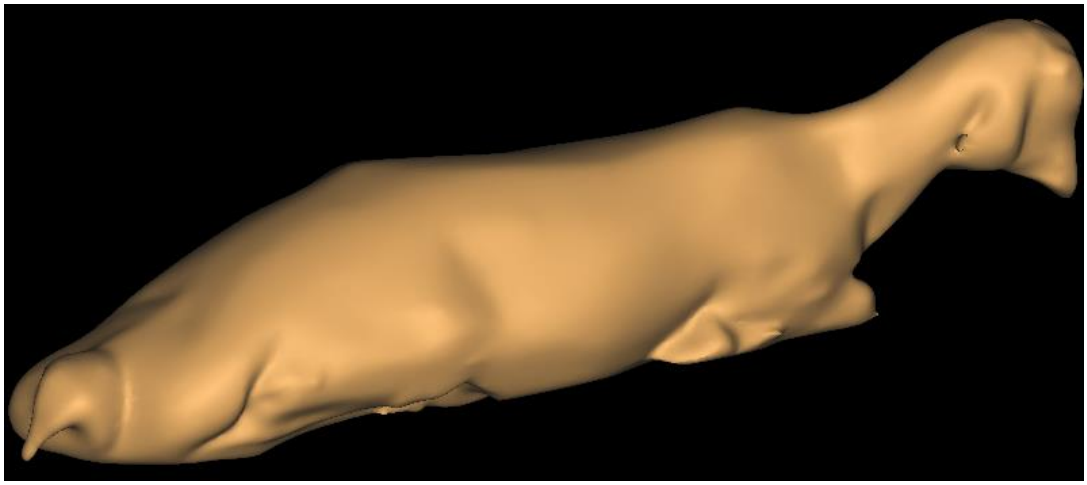

**Figure 23** A 3D view of the whole-body homogeneous sheep model

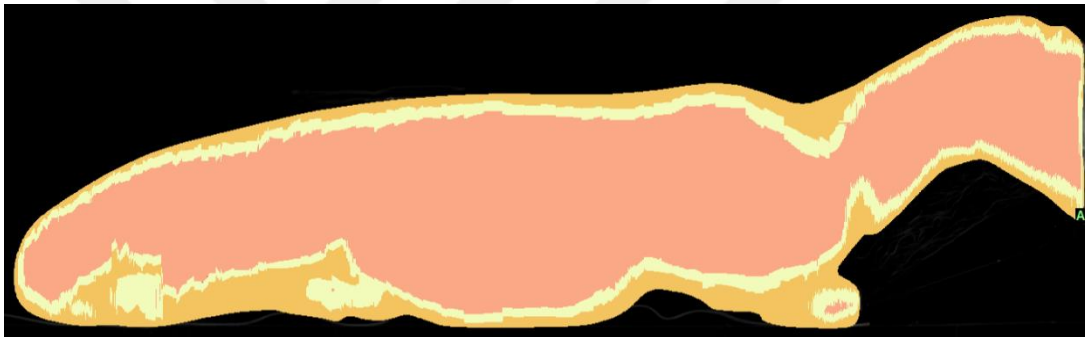

**Figure 24** Three-layered segmented mask of a full body sheep

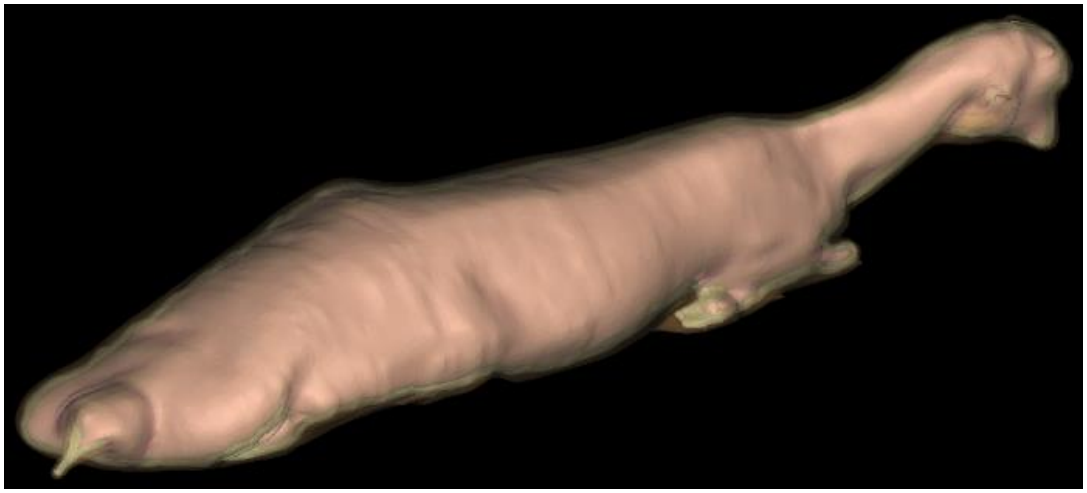

**Figure 25** A 3D view of the three-layered sheep model

Finally, we segment seven-tissues which are brain, bone, skin, fat, muscle, eye and internal air. We use threshold function to segment some tissues. Threshold function works very well especially on bone tissue as it can be seen in Figure 26.

**Figure 26** A 3D view of the segmented sheep bone

To select all pixels inside the body, after segmenting some tissues, we subtract the tissues from the homogeneous model which is fully segmented as muscle tissue. Then, we segment all seven tissues as in Figure 27. The color bar that refers to tissues is shown in Figure 28.

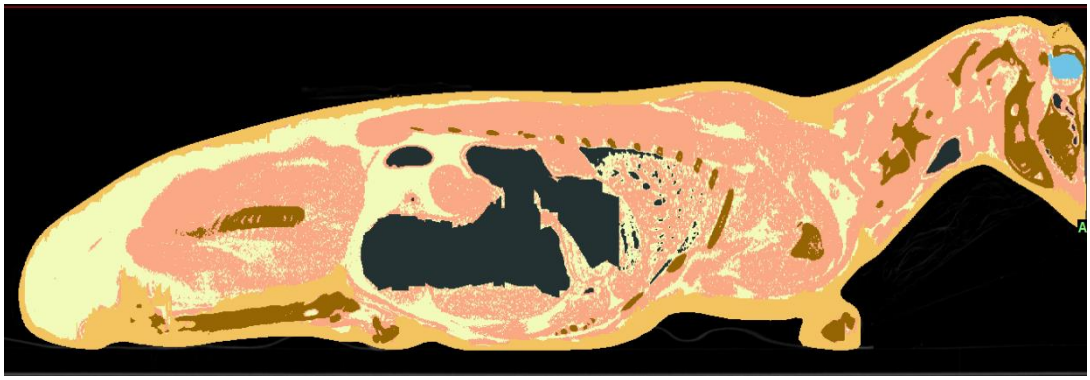

**Figure 27** Seven-tissues segmented mask of a full body sheep


**Figure 28** Color map for the tissues of whole body model

**Figure 29** A 3D view of whole-body anatomic sheep model

After segmentation of the seven tissues, we generate 3D model and obtain the anatomic model as shown in Figure 29. When the models are ready for simulation, we export them in STL (abbreviated from standard triangle language) format which is proper for the Sim4Life [17] software.

# CHAPTER 3

## SAR AND BIO-HEAT SIMULATIONS

After inventions of 3T and higher-field MRI scanners, an increasing concern related to heating effects of MRI body coils has been started [8–18]. Because of the effects of electromagnetic waves generated by RF coils, the core temperature of the body inside the coil may increase, or local hot spots may occur. For the small surface coils that deliver less power compared to body coils, local heating can be dangerous [21]. For body coils that are generally built in the scanner, recent studies on swine show that when scan durations exceed 15 minutes, there can be significant increase in the core-body temperature [8], [10], [19].

To ensure safety and limit power output of RF coils, standards have been published by the international electrotechnical commission (IEC) [24]. The main concern in RF safety is about heating, but because of difficulties of calculating in-vivo heating, safety standards are set in terms of specific absorption rate (SAR), which is a measure of the absorbed power. The point-wise SAR is defined as

$$\mathrm{SAR}(\mathbf{R}) = \frac{\sigma(\mathbf{R})\left\|\mathbf{E}(\mathbf{R})\right\|^2}{\rho(\mathbf{R})}, \tag{3.1}$$

where $\sigma$ is conductivity $(\mathrm{S/m^2})$ and $\rho$ is density $(\mathrm{kg/m^3})$ of the tissue. However, for local SAR, an averaged version of (3.1) is used, i.e.,

$$\mathrm{SAR_L} = \frac{1}{V}\int_{10\,\mathrm{gr\,sample}} \frac{\sigma(\mathbf{R})\left\|\mathbf{E}(\mathbf{R})\right\|^2}{\rho(\mathbf{R})}\, d\mathbf{R}. \tag{3.2}$$

where $V$ is a sample volume that weighs 10 gr. That local limit needs to be ensured for surface coils. However, for volume coils, such as the ones built in MRI scanners, a whole or partial body averaged version of SAR is used, where the output power is simply divided by the imaged part of the body. The current limits of IEC are shown in Table 1.

Note that when an average person of 80 kg is scanned for whole body MRI, he/she can get 160 W (320 W in controlled mode) of power which is about an order of magnitude higher than powers generated by cellular phones. However, in this calculation, we assume that all power delivered from RF coils is absorbed by the body. In reality, such 100% efficiency does not exist and some percentage of the power is lost.

| **SAR Limits** ***(W/kg)*** | Average SAR ($SAR_A$) | | Local SAR ($SAR_L$) (10 g. average) | | |
|---|---|---|---|---|---|
| | Whole Body | Head | Head | Trunk | Extremity |
| Normal Mode | 2 | 3.2 | 10 | 10 | 20 |
| First Level Controlled Mode | 4 | 3.2 | 20 | 20 | 40 |

**Table 1** IEC SAR Limits for MRI

In this study, we address MRI safety in a 3 T scanner by comparing SAR and temperature increase in anatomic sheep models with increasing complexity. We prefer to study with sheep so that we can compare simulation results with animal experiments, which are explained in Chapter 5.

For safety of the body scanned with MRI a foresight should be obtained about in-vivo temperatures. Temperatures in a tissue with blood vessels having diameters smaller than one mm can be determined using approximate thermal models of the body [25]. Temperatures in blood vessels having larger diameter than one mm are determined the convective energy equation (CEE) using exact thermal model [25].

The Penne's bio-heat transfer model (BHTM) [26], [27] is widely used to calculate in-vivo temperatures. BHTM describes heat transfers between blood and tissues assuming that blood is an infinite sink and core-body temperature does not increase. The parameters and variables used in BHTMs are empirical and are not clearly defined [25]. Thus, new models have been proposed which try to overcome

such deficits [25], [28]–[31]. Here, we consider the generic bio-heat transfer model [32] which considers the core-body heating. We refer to this method as generalized bio-heat transfer model (GBHTM).

For our MRI coil simulations, we use Sim4Life software that calculates point-wise and local peak SAR values. Parallel and GPU implementations of FDTD method allows fast calculations. Sim4Life also calculates temperature increase using BHTM. They provide electrical and heat parameters of different body tissues from a well-known database [33]. Those values at 128 MHz, the resonance frequency of 3T coils, are shown in Table 2.

| **Tissue** | $\sigma$ | $\varepsilon_r$ | $\rho$ | $c$ | $k$ | $w$ |
|---|---|---|---|---|---|---|
| Muscle | 0.72 | 63.49 | 1090 | 3421 | 0.49 | 36.7 |
| Skin | 0.52 | 65.44 | 1109 | 3390 | 0.37 | 106.4 |
| Fat | 0.07 | 12.37 | 911 | 2348 | 0.21 | 32.7 |
| Bone | 0.07 | 14.72 | 1908 | 1312 | 0.32 | 10.0 |
| Brain | 0.83 | 79.74 | 1045 | 3630 | 0.51 | 558.6 |
| Eye | 1.51 | 69.06 | 1004 | 4047 | 0.59 | 0.0 |
| Internal air | 0.00 | 1.00 | 1.20 | 1003 | 0.03 | 0.0 |
| Note: $\sigma$ is conductivity (S/m), $\varepsilon_r$ is relative permittivity (dimensionless), $\rho$ is density (kg/m^3), $c$ is heat capacity (J/kg/K), $k$ is thermal conductivity (W/m/K), and $w$ is perfusion rate (ml/kg/min). | | | | | | |

**Table 2** Tissue Parameters for SAR and heat calculations

As is well-known, FDTD method is a direct solution of time-domain Maxwell's equations. The electric-field (E) and magnetic-field (H) components are allocated in space on a staggered mesh of Cartesian coordinate system as shown in Figure 30. E and H components are updated in a leap-frog scheme according to finite-difference scheme. The transient fields can be calculated when the initial field, boundary and source conditions are known. Hence, wide-band simulations can be

performed easier with FDTD compared to frequency-domain methods, such as MOM or FEM.

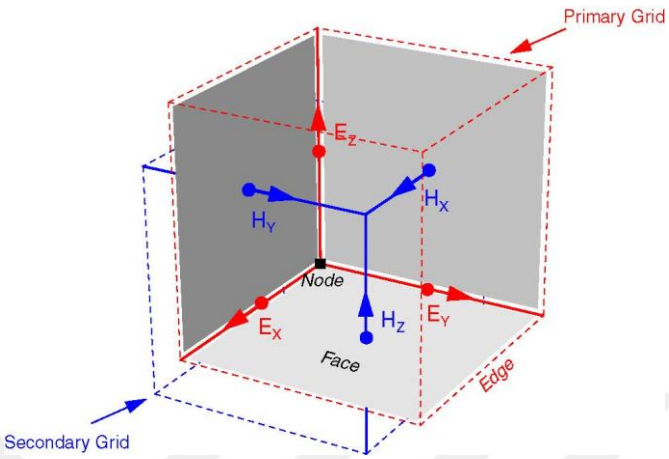


**Figure 30** E and H components in staggered grid

To truncate the computational domain in a sufficient manner, Sim4Life provides an absorbing boundary condition, which is closely related to Berenger's perfectly matched layer [34]. It is also possible to truncate the domain using perfectly conductive boundary conditions, in which tangential components of the E-fields on the outer boundaries are set to zero. That feature is used to model metal shields of RF coils.

## 3.1 Verification

For verification purposes, we first review a paper [35] which has detailed MRI simulations with FDTD at 64 MHz and at 200 MHz. Here, we also used FEKO software [36] that is based on MOM and FEM. Moreover, FEKO supports a hybrid method (FEM/MOM), which can work efficiently with complex heterogeneous structures that includes metallic surfaces.

The simulations are performed with a birdcage coil and two different phantoms as shown in Figure 31. The birdcage coil has 29 cm diameter, 40 cm length and 16 struts. The cylindrical phantom has 19.6 cm diameter, 22 cm length and the octagonal phantom has 20.7 cm diameter, 40 cm length. To tune the birdcage to resonance frequency, there are capacitors located between each strut at top and bottom of the birdcage coil.

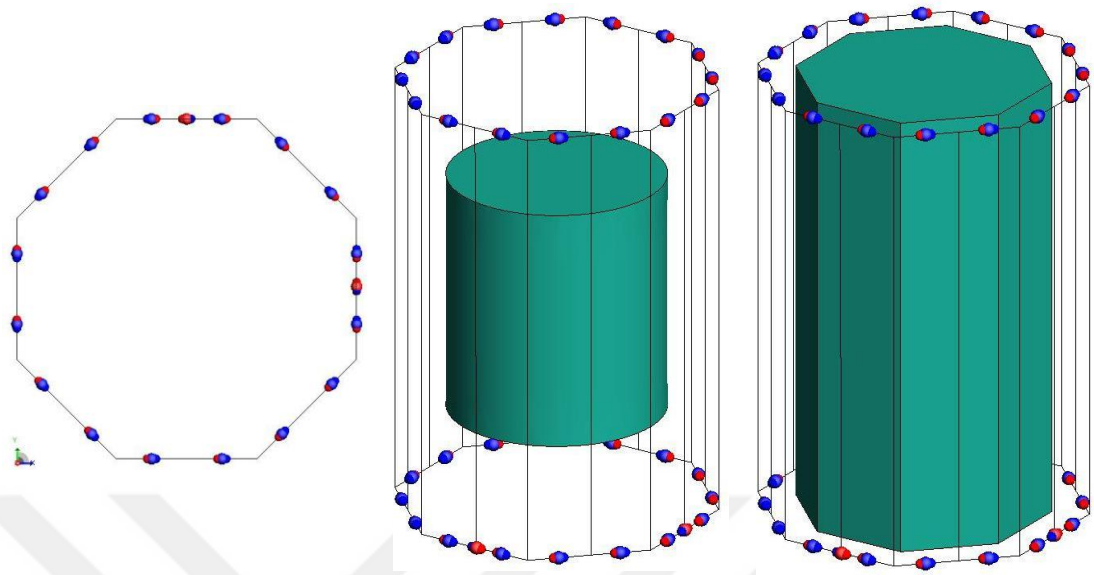

a) Top view of the coil b) Cylindrical phantom c) Octagonal phantom

**Figure 31** A 16 struts birdcage model with phantoms

First, to find the value of the tuning capacitor we performed wideband simulations on FEKO and Sim4Life with different capacitor values. The resonance reactions of the coil for 64 MHz (1.5 T frequency) and 128 MHz (3 T frequency) are shown in Figure 32. The tuning capacitor values were close to each other for FEKO and Sim4Life simulations. However, we note that there is significant loading effect for 128 MHz simulation and the resonance frequency shifts with loading.

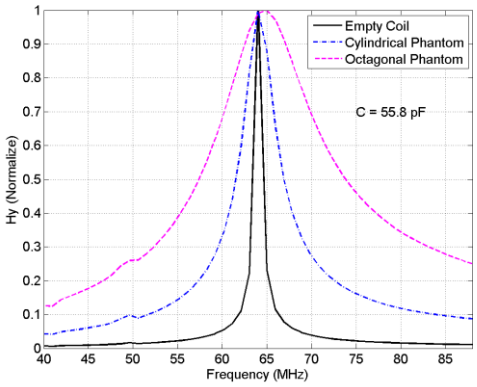


a) 64 MHz by FEKO

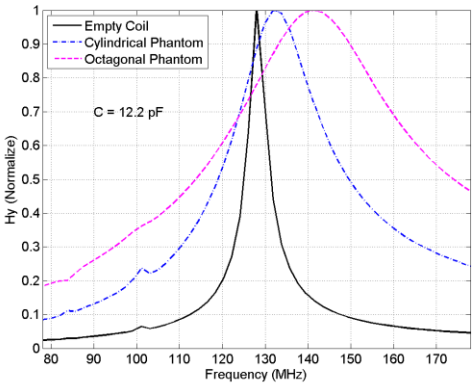


b) 128 MHz by FEKO

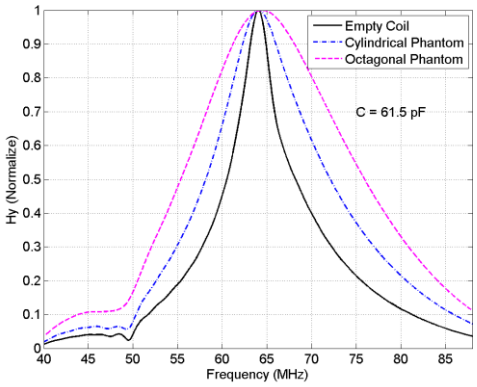


c) 64 MHz by Sim4Life

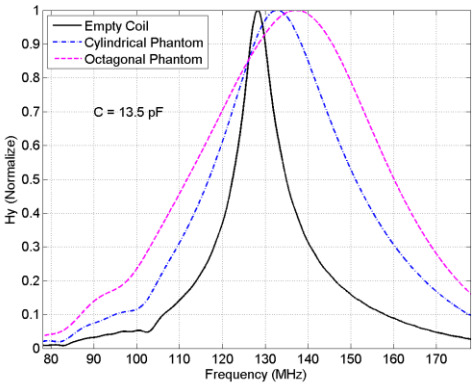


d) 128 MHz by Sim4Life

**Figure 32** Responses of resonances at 64 MHz and 128 MHz

When we analyze B1 (right-hand circularly polarized portion of the transmitted magnetic field) and SAR plots of these simulations, we observe that homogeneity of B1 decrease with the effect of phantom at 128 MHz compared to 64 MHz as can be seen in Figure 33. Distributions of B1 on two lines are also presented in Figure 34.

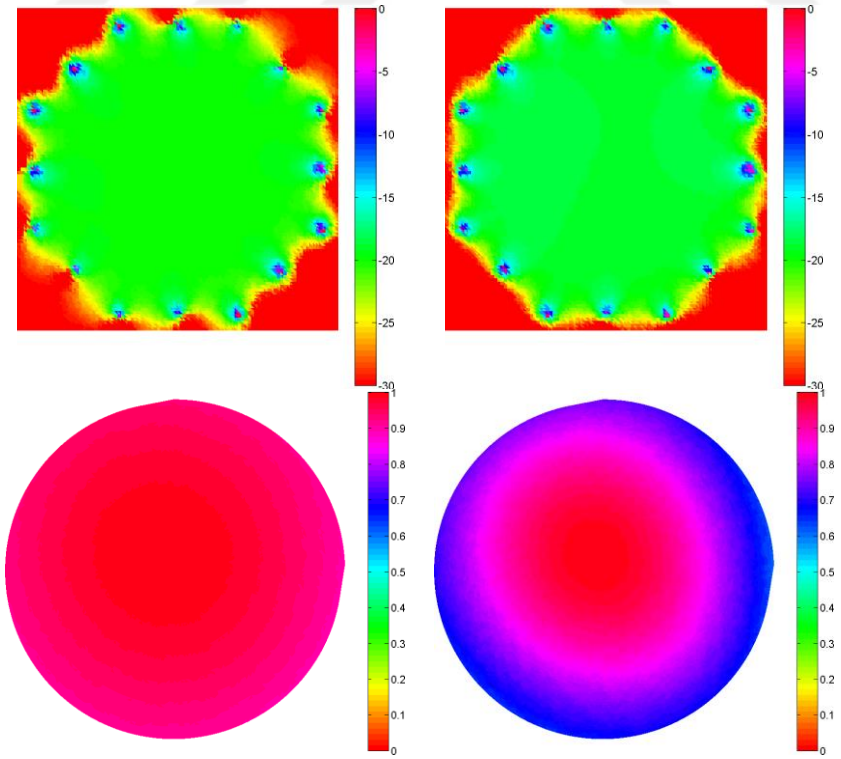

**Figure 33** B1 plots for empty (top) and cylindrical phantom (bottom) at 64 MHz (left) and 128 MHz (right)

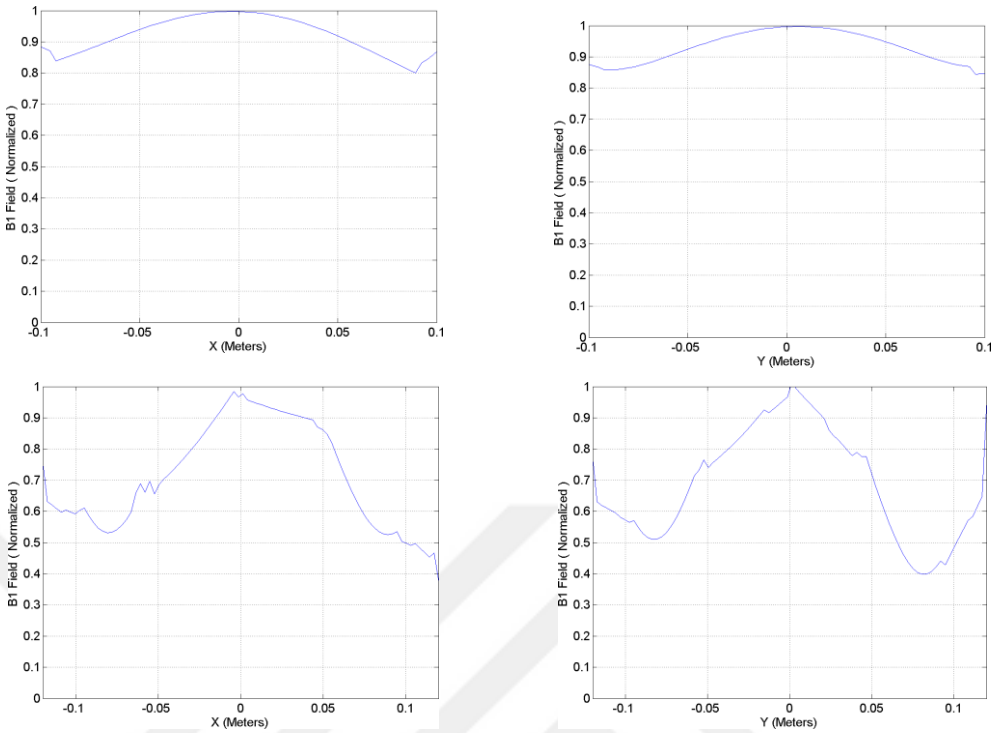


**Figure 34** The distribution of B1 field on z = 0, y = 0 (x-axis) and z = 0, x = 0 (y-axis) for 64 MHz (top) and 128 MHz (bottom)

## 3.2 Simulations for the Head and Neck Model with a Head Coil

After the verification of our setup and determination of tuning capacitors, we perform SAR simulations on phantom and head and neck model of the sheep. There are local SAR results and location of peak average SAR (1 gr) normalized to 1 W source power in Figure 35. The value of peak SAR is about 0.4 W/kg. Since the phantom weight is about 13 kg and max average SAR can be 3.2 W/kg for head isocenter in IEC limits, the total power allowed can be 41.6 W. Then, the local SAR is 16.6 W/kg for this power level, significantly exceeding the 10 W/kg local limit of IEC for head.

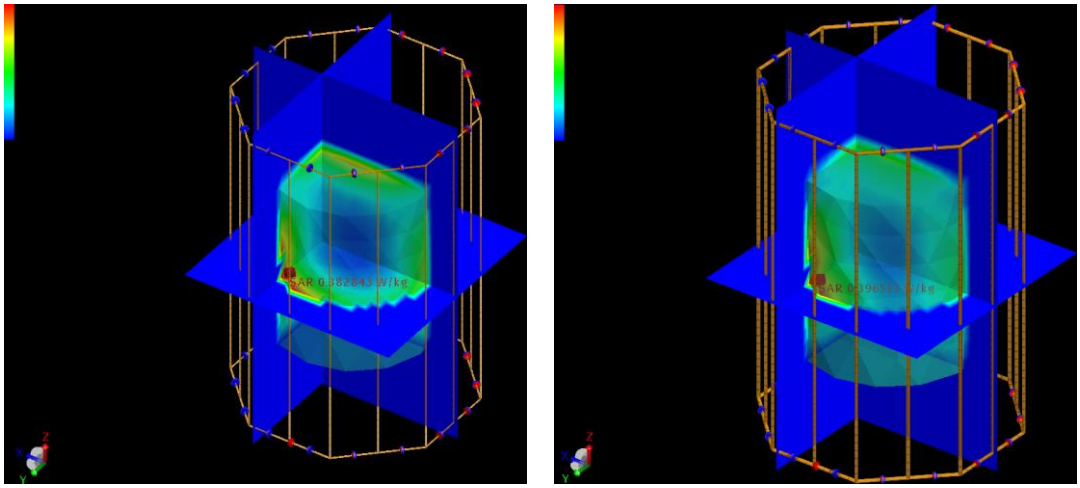

a) 64 MHz b) 128 MHz

**Figure 35** SAR results of cylindrical phantom

SAR results of the homogeneous head model of sheep are given in Figure 36. The peak SAR values are 0.59 W/kg at 64 MHz and 0.64 W/kg at 128 MHz. When we set the source power 105 W as in the experiments (which corresponds to average SAR of approximately 3 W/kg), the peak SAR value will be about 60 W/kg. If we assume that 80 % of power is absorbed by the sheep, this means that peak SAR is abot 48 W/kg and again is extremely beyond the IEC limit. These results are in agreement with the previous studies, e.g., [37], [38].

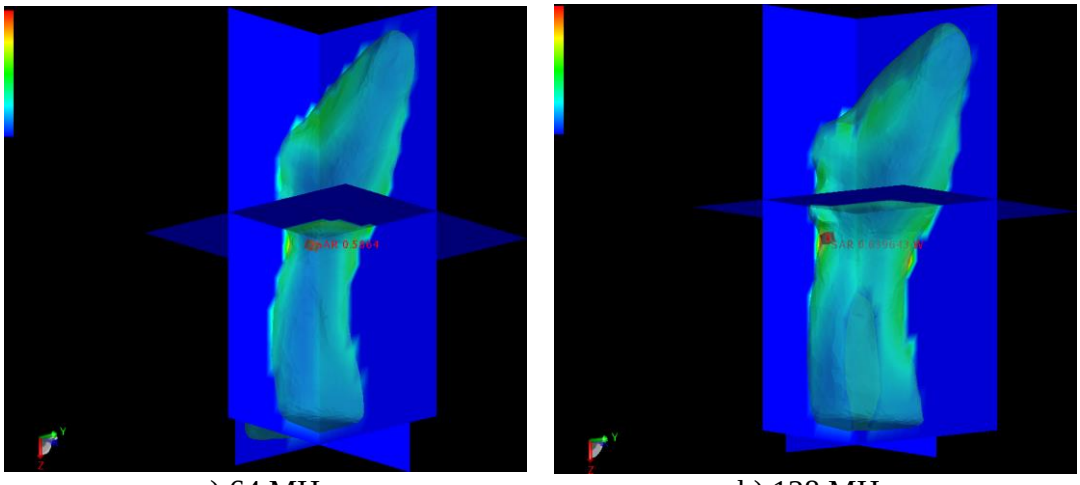

a) 64 MHz b) 128 MHz

**Figure 36** SAR results of homogeneous head model of the sheep

### 3.3 Simulations for the Whole-Body Model with a Birdcage Body Coil

As shown in Figure 37, we consider two scenarios for the location of the sheep in the MRI scanner. First, trunk is located at the iso-center, and second, head is at the iso-center of the MRI scanner. When, trunk is at the iso-center, the whole body is in the field-of-view of the scanner, and more power compared to head iso-center case can be delivered by RF coils. The IEC limit is 2 W/kg in this case. When head is at the iso-center, only a portion of the body, i.e., head and neck, is in the field-of-view and the IEC limit is 3.2 W/kg.

We use a 16 channel birdcage coil which is typically used in 3T MRI scanners [39]. The coil has 60 cm diameter and 40 cm length. The metal shield covering the coil has 68 diameter and 1 m length. The coil is driven in quadrature mode. We use Sim4Life software for SAR and bio-heat simulations. We also use a code that implemented GBHTM [32].

We model the birdcage coil and shield using Sim4life. Then, we describe the sources and capacitors on the birdcage coil. To find the tuning capacitor value, we run with empty coil using different capacitor values. For the birdcage and shield that we used, the tuning capacitor value is 11.5 pF (Figure 38). Next, we import the models which are created and exported from MIMICS as a STL file (Figure 39) and assign tissue parameters properly. Then, we locate the model inside of the coil as head is at the iso-center and body is at the iso-center.

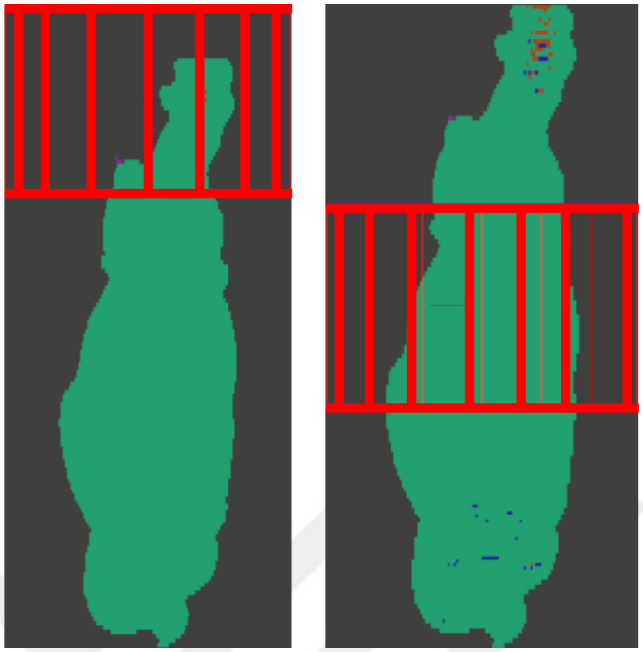

a) Head iso-centered b) Body iso-centered

**Figure 37** Two different simulations scenarios in MRI scanner

In total, we have six cases for simulation. Those are homogeneous, three-layered and anatomic (seven-tissues) sheep models either head is at the iso-center or body is at the iso-center. At the same time, we perform six more bio-heat simulations for each case.

The models are exported from MIMICS at 5.1 mm x 5.1 mm x 1.2 mm resolution and we discretize the models at 3 mm x 3 mm x 5mm resolution which yields approximately 15 million voxels (Figure 40). These resolutions are required in order to model small organs such as eye.

After the grid is generated and voxels are created as in Figure 41, it is ready to simulate and we run the solver respectively in a Windows server that hosts 2 Intel Xeon CPU E5-2650 2.60 GHz. Each one of the run takes almost 25-30 hours. We note that simulations could be performed much faster using GPU implementation of Sim4Life.

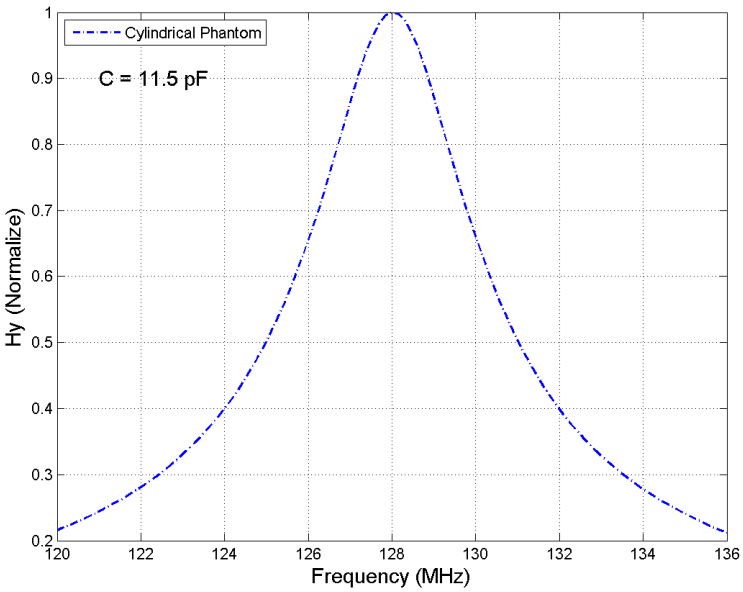


**Figure 38** Response of resonance for the body coil

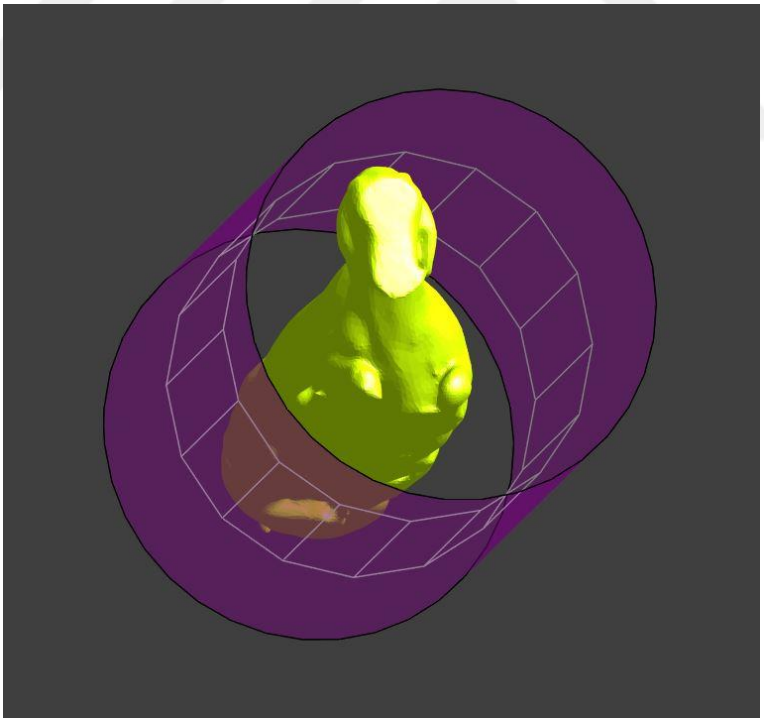

**Figure 39** Imported STL model

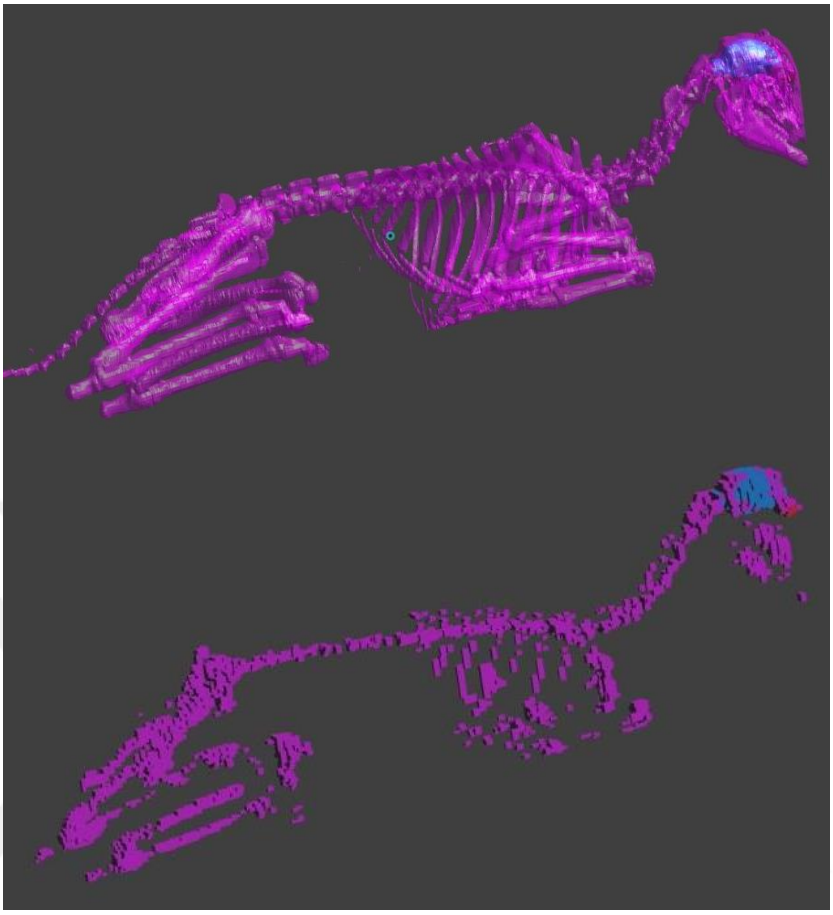

**Figure 40** Imported sheep models: Bone, brain, and eye tissues imported from MIMICS (top) and voxelized model (bottom)

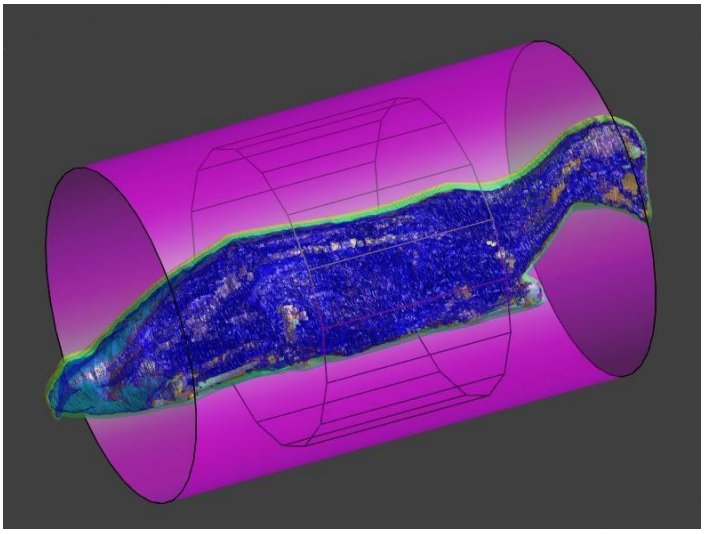

**Figure 41** Voxel view of the sheep model

For the bio-heat simulations, we set the duration of RF pulse as one hour as in the in-vivo experiments. The results belonging to body iso-centered case is shown in Figure 42. SAR results are normalized to 1W power. For bio-heat simulations, the input power is assumed to be 100 W which corresponds to approximately 2W/kg SAR for an average sheep. For the homogeneous case (Figure 42.a and b) we note that SAR and temperature results are closely related and the final temperature distribution is merely a diffused version of SAR, as can be predicted from the BHTM model.

The three-layer model (Figure 42.c and d) overestimates SAR and temperature but the results are closer to those of anatomic model (Figure 42 e and f) when compared to the homogeneous model. For the heterogeneous model, we observe that when the results are normalized to a whole-body SAR value of 2 W/kg, peak point-wise SAR gets close to 80 W/kg. Peak SAR results and temperature increase rates for the body isocenter case are shown in Table 3. The SAR results, are again, consistent with the literature [37], [38], [40] and severely exceeds local safety limits. In that table we also show temperature increase per watt per hour and expected temperature increase for a typical MRI exam. According to those results, the body temperature can increase 3 $^{o}$C for a 30-minute scan, which is a worrisome result.

Finally, in Figure 43, we compare solvers using BHTM with GBHTM. As will be revealed in the next Chapter, GBHTM results agree better with experimental findings and the reason is that BHTM underestimates the heating by assuming constant body temperature during the scan.

For the second case in which the head of the sheep is at the iso-center of the scanner, the results are displayed in Figure 44. In this case, computed peak local SAR values are 83.8 W/kg, 23.4 W/kg, and 54.4 W/kg for the homogeneous, layered, and seven-tissues models, respectively. For the axial slice shown that pass through eyes and brain, we see similar results to those of body isocenter case except that temperature increase is less in this case. If we assume that exposed part of the sheep weighs half of the total weight then the maximum input power will be 80 W which yields about 2 $^{o}$C increase for the head.

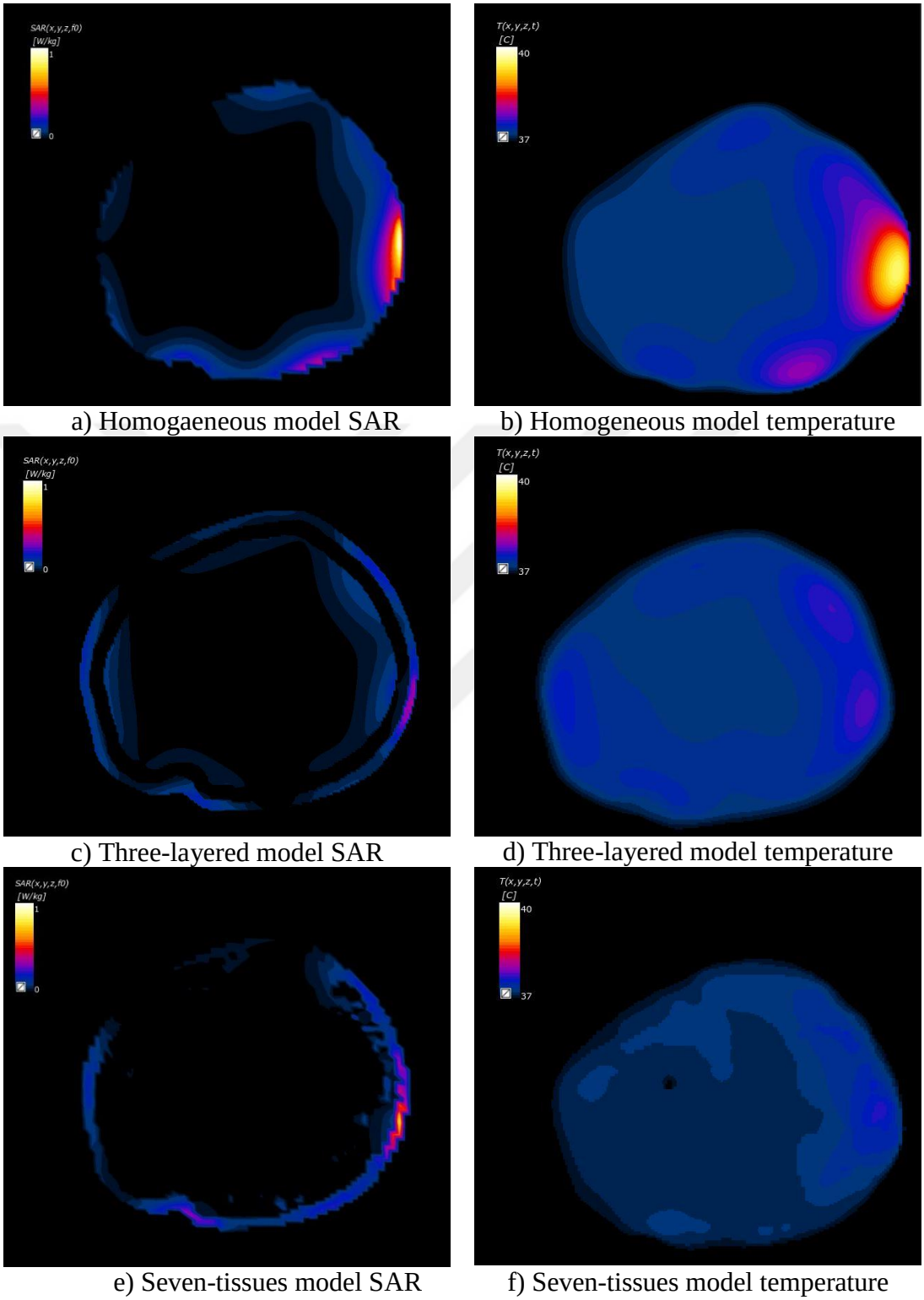


a) Homogaeneous model SAR b) Homogeneous model temperature

c) Three-layered model SAR d) Three-layered model temperature

e) Seven-tissues model SAR f) Seven-tissues model temperature

**Figure 42** Body iso-centered SAR and temperature simulations by Sim4Life

| | **Homogeneous Model** | **Three-layered Model** | **Seven-Tissues Model** |
|---|---|---|---|
| 10 gr peak SAR (W/kg) | 134 | 43 | 84 |
| $\Delta T$ ($^oC$/W/hr) | 0.15 | 0.05 | 0.06 |
| $\Delta T$ for 30 min scan ($^oC$) | 7.5 | 2.5 | 3 |

**Table 3** Local SAR results obtained with the body iso-center case

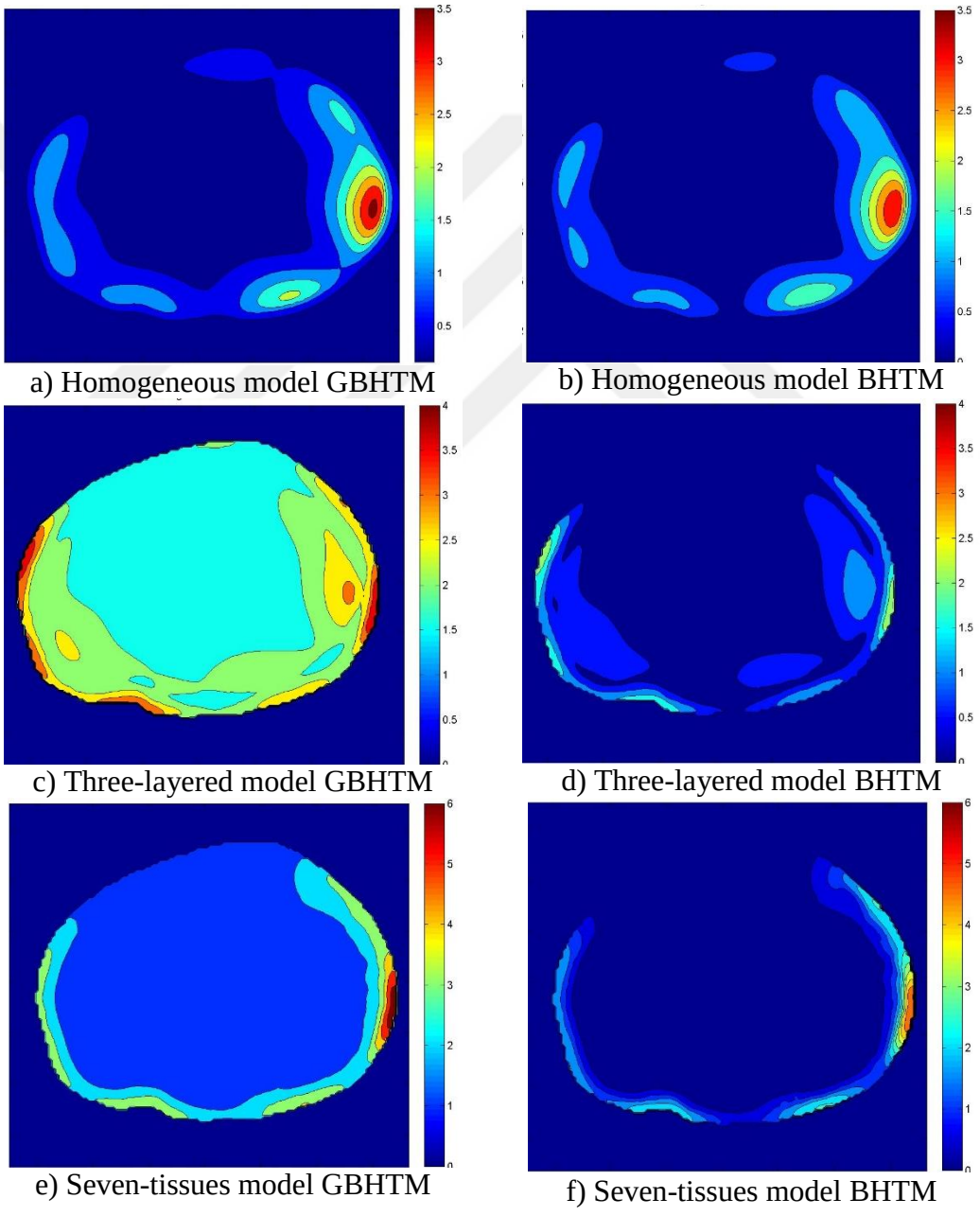

a) Homogeneous model GBHTM b) Homogeneous model BHTM

c) Three-layered model GBHTM d) Three-layered model BHTM

e) Seven-tissues model GBHTM f) Seven-tissues model BHTM

**Figure 43** Bio-heat simulations using GBTHM and BHTM

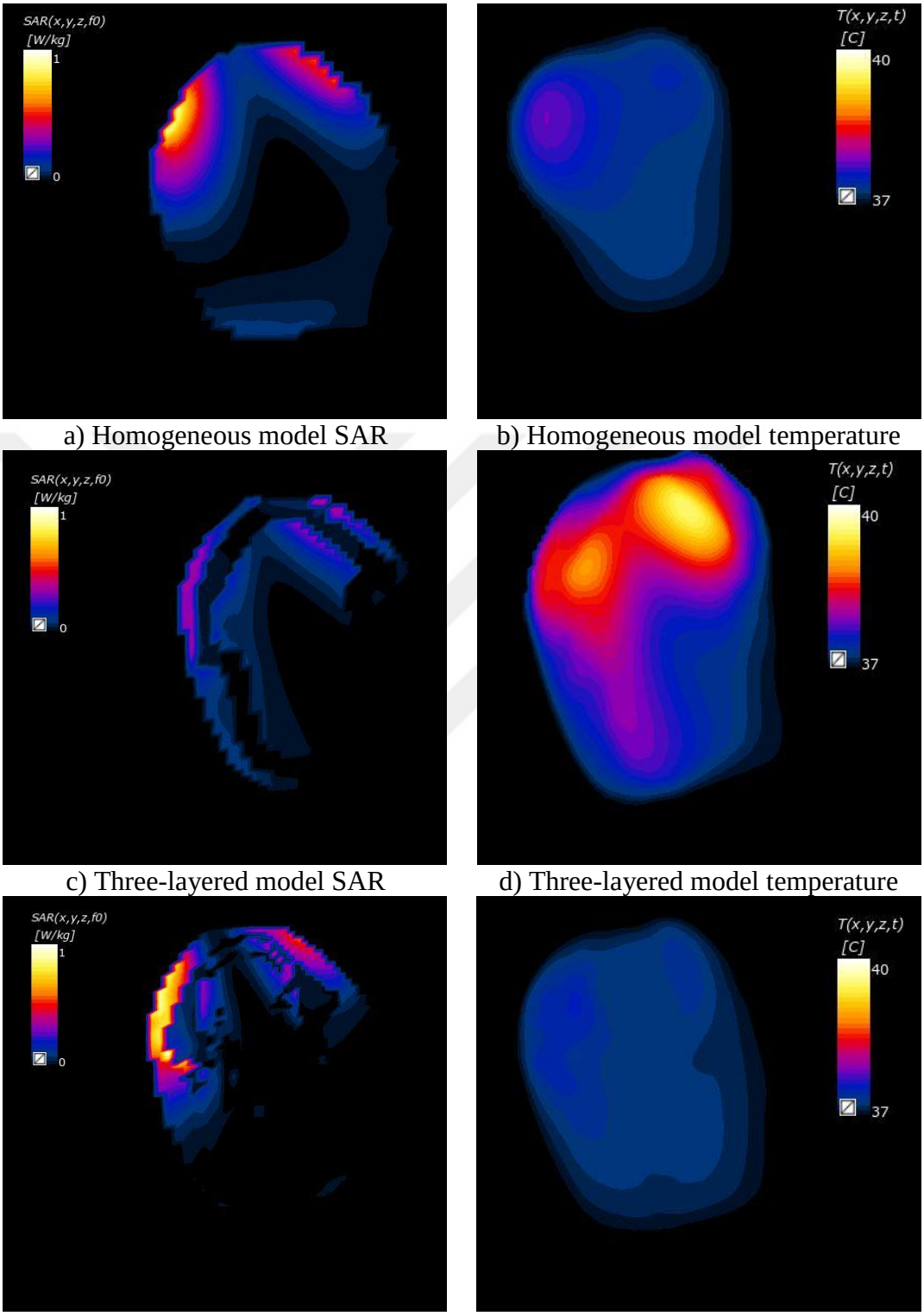


a) Homogeneous model SAR b) Homogeneous model temperature

c) Three-layered model SAR d) Three-layered model temperature

e) Seven-tissues model SAR f) Seven-tissues model temperature

**Figure 44** Head iso-centered SAR and temperature simulations with Sim4Life

# CHAPTER 4

## ANIMAL EXPERIMENTS

The required ethical approval for sheep experiments is obtained from Bilkent University ethical committee. We make four sheep experiments with five sheeps. The animals are transported to the laboratory for 24 hours before the test and are stopped eating. Premedication is achieved by injecting firstly 0.02 mg/kg, sc, Atropine (%0.2 Atropine), after 20 minutes 0.5 mg/kg, im, Xylazine HCl (%2 Alfazine) to about 50-60 kg animals for general anesthesia. 5 minutes after Xylazine HCl injection, 2.5 mg/kg, im, Ketamine HCl (%10 Ketasol) is injected for induction of anesthesia. After waiting 10 minutes, 24 G intracath is placed to ear vein (vena auris) of the sheep by performing intubation with 7.5 cuffed endotracheal tube.

Continuation of anesthesia is performed with TIVA (Total Intravenous Anesthesia). Implementation period of TIVA is set at 45 minutes after injection of Atropine. For this purpose, 16 mg/kg Propofol (%1 Pofol) is added in 230 ml saline solution as infusion method in the form of 0.16 mg/kg/min dose. Safe and deeply anesthesia is achieved for about 4-5 hours by this process. The first two hours are required for the surgical intervention and to insert heat probes to various parts of the body. To measure the temperatures, we place temperature probes to body and head of anesthetized sheep. Then, for half an hour pre-scan temperature is recorded to see the effects of anesthesia. Then RF power is applied for one hour. Finally, post-scan time is recorded for half an hour. Then, sheep are euthanized in accordance with the ethical requirements.

Our first experiment is performed with two sheeps; one is for body iso-centered and the other is for head iso-centered. For body iso-centered experiment, the probes are placed to hypodermic, 2 cm and 5 cm deep in muscle and rectum. For head iso-centered experiment, the probes are placed to hypodermic, 2 cm and 5 cm deep in brain and rectum.

For body iso-center experiment, total source power is 227 W and whole-body SAR is 3.5 W/kg for the 65 kg sheep. For head iso-centered experiment, total source power is split to half and whole body SAR is 1.6 W/kg.

The temperature results are shown in Figure 45 for body iso-centered and in Figure 46 for head iso-centered. The vertical lines show the start and end time of RF wave. We can see there are 2°C temperature increase for body iso-centered and 1°C temperature increasing for head iso-centered experiments.

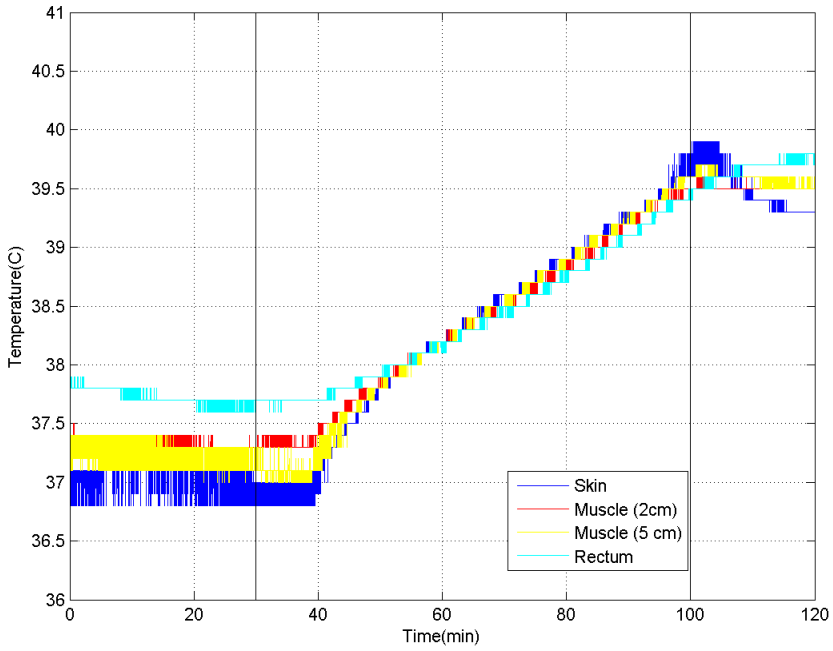


**Figure 45** Temperature results for the first experiment in which body is at the iso-center

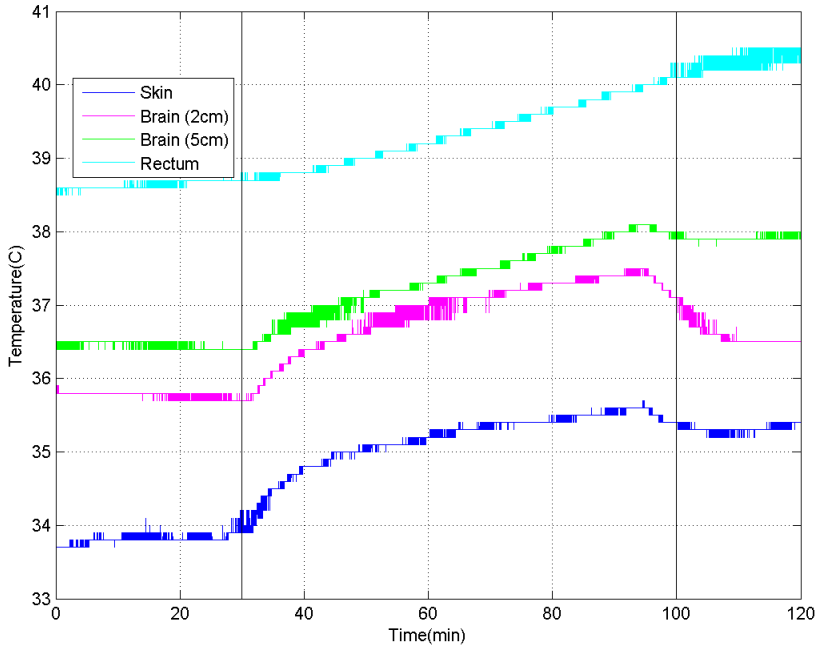


**Figure 46** Temperature results for the first experiment in which head is at the iso-center

The second experiment is performed with a 50 kg male sheep and head was at the iso-center. Anesthesia is performed successfully as in the first experiment. The probe is inserted 2 cm deep in the brain. The results, which are consistent with the first experiment, is displayed in Figure 47.

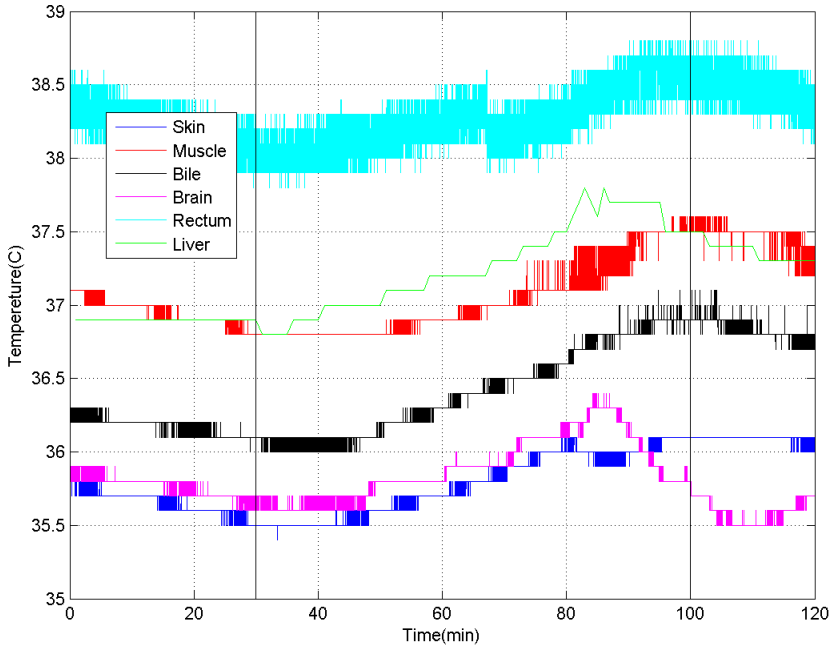


**Figure 47** Temperature results for the second experiment in which body is at the iso-center

The third experiment is performed again with a 48 kg male sheep. The probes are placed in hypodermic, muscle, bile, brain and rectum for body-core mesurement. The scan is started with body is iso-centered. The total source power is 136 W and average SAR is 2.83 W/kg. The temperature results are shown in Figure 48. We can see about 3-4°C temperature increasing. We also observe that the sheep has not comfortable respiration during anesthesia and it sneezes often. It has probably a respiratory tract infection. There are increasing temperatures before and after RF waves. The temperatures are not balanced as in previous experiments. This shows that MRI may damage unhealthy individuals. However, we note that MRI scanners are used without any distinction between healthy or unhealthy persons.

Finally, we depict the results for the final experiment in Figure 49, in which body of the sheep is located at the iso-center. In that experiment, one of the main arteries of the brain was injured during surgical intervention. Hence, we did not wait for half an hour before the RF power. Nonetheless, the experiment ended successfully and the results turned out to be in consistent with the previous ones.

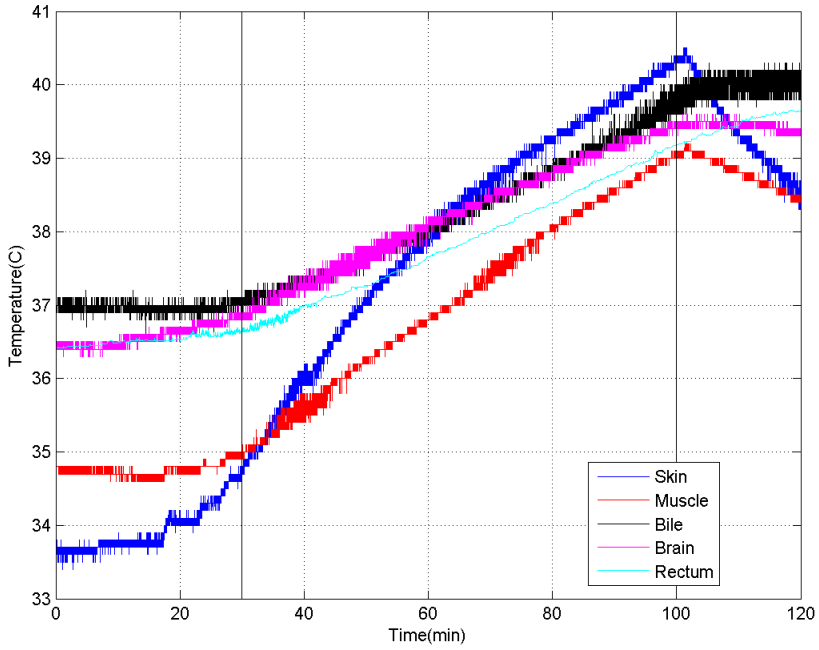


**Figure 48** Temperature results for the third experiment in which body is at the iso-center

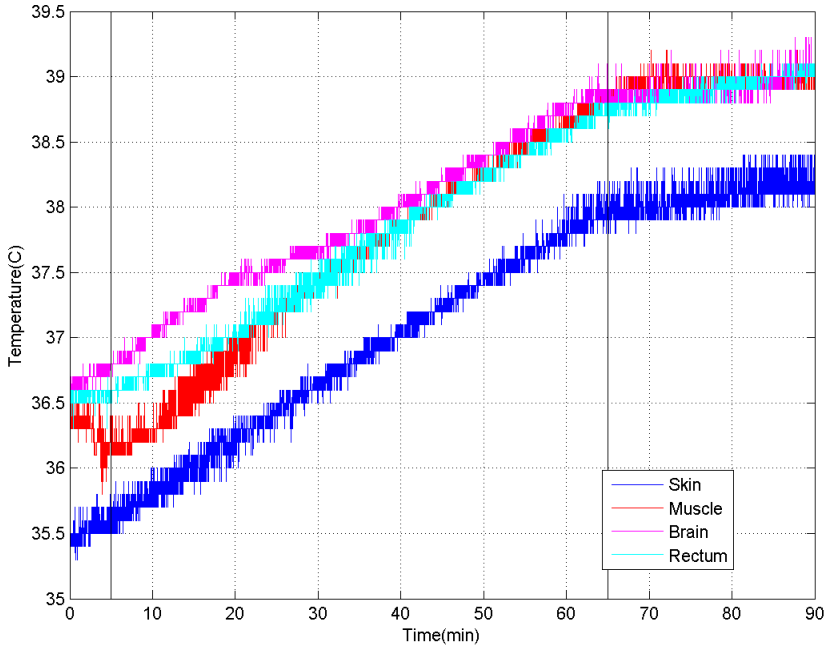


**Figure 49** Temperature results for the fourth experiment in which body is at the iso-center

# CHAPTER 5

## CONCLUSION

This thesis is a part of an ongoing project which aims to explain some questions about MRI safety. The ultimate aim is to accurately find SAR and temperature distributions of human body when exposed to RF fields of MRI coils. However, there are significant challenges needs to be overcome to reach that goal.

First of all, the SAR distributions, which are input to the bio-heat solver, need to be accurately computed. Even though electromagnetic theory and solvers are mature and can provide error-controlled solutions, the physical problem that we address is fairly complicated and hard to repeat exactly. The detail of the anatomic model, the orientation of the model in the coil, finite-elements used for the discretization of the model (e.g., voxels, tetrahedrons, or higher-order elements), and solvers have the potential effect to change the results significantly. Even though the error sources that may occur because of those effects are minimized, a single anatomic model cannot be always a good representative for all patients.

For the bio-heat modeling, the situation is even worse. The basic assumption of constant body-temperature for commonly used BHTM is apparently wrong for the body coils. There are efforts to develop better models, but none of them has been proven to be both successful and practical. Furthermore, the thermo-physical responses, i.e., sweating, heart-rate changes, vasodilatation, are all important but very difficult to incorporate in bio-heat solvers.

As an attempt to reach the ultimate goal mentioned above, this thesis found the answers of some questions. The experiments revealed that for scans, those are longer than 15 minutes, core-body heating cannot be ignored and a method that does not ignore body-heating, such as GBHTM, should be the method of choice for such situations. When computational time is concerned, for example considering the efforts to ensure have individualized safety [23], three-layer models can be used for fast calculations. However, homogeneous models significantly overestimate heating

and can be too protective and limit the progress of high-field MRI that requires as much possible power as possible for high-quality scans [41].

Many of the questions are yet to be answered. First of all, MOM/FEM hybrid solvers can provide more accurate and efficient SAR solutions due to better and more flexible modeling opportunities and superiority of the solver. The effects of anatomic details and relative location of the model in the coil are important factors that affect accuracy of solutions. Related to bio-heat solvers, GBHTM is a promising one but it needs to be used by more researchers and get more mature. Once confidence with the electromagnetic and bio-heat solvers is achieved with the help of the animal experiments, the simulations need to be performed on the human body. In that case, one must consider that thermoregulatory systems of human may have some significant differences compared to animals.

## REFERENCES


[1] F. G. Shellock and J. V. Crues, “Corneal temperature changes induced by high-field-strength MR imaging with a head coil.,” *Radiology*, vol. 167, pp. 809–811, 1988.

[2] F. G. Shellock, D. J. Schaefer, and J. V. Crues, “Exposure to a 1.5-T static magnetic field does not alter body and skin temperatures in man,” *Magn. Reson. Med.*, vol. 11, no. 3, pp. 371–375, Sep. 1989.

[3] F. G. Shellock, *Magnetic resonance procedures : health effects and safety*. Boca Raton: CRC Press, 2001.

[4] F. G. Shellock, “Radiofrequency Energy-Induced Heating During MR Procedures: A Review,” *J. Magn. Reson. Imaging*, vol. 12, no. 1, pp. 30–36, Jul. 2000.

[5] Shellock and J. V. Crues, “Temperature changes caused by MR imaging of the brain with a head coil.,” *AJNR*, vol. 9, pp. 287–191, 1988.

[6] F. G. Shellock, “Thermal Responses in Human Subjects Exposed to Magnetic Resonance Imaging,” *Ann. N. Y. Acad. Sci.*, vol. 649, no. 1 Biological Ef, pp. 260–272, Mar. 1992.

[7] “Thermal effects of MR imaging: worst-case studies on sheep.,” *Am. J. Roentgenol.*, vol. 155, no. 5, pp. 1105–1110, Nov. 1990.

[8] D. Shrivastava, L. Utecht, J. Tian, J. Hughes, and J. T. Vaughan, “In vivo radiofrequency heating in swine in a 3T (123.2-MHz) birdcage whole body coil: In Vivo RF Heating in 3T,” *Magn. Reson. Med.*, vol. 72, no. 4, pp. 1141–1150, Oct. 2014.

[9] D. Shrivastava, T. Hanson, J. Kulesa, L. DelaBarre, P. Iaizzo, and J. T. Vaughan, “Radio frequency heating at 9.4T (400.2 MHz): In vivo thermoregulatory temperature response in swine,” *Magn. Reson. Med.*, vol. 62, no. 4, pp. 888–895, Oct. 2009.

[10] D. Shrivastava, T. Hanson, J. Kulesa, J. Tian, G. Adriany, and J. T. Vaughan, “Radiofrequency heating in porcine models with a ‘large’ 32 cm internal diameter, 7 T (296 MHz) head coil,” *Magn. Reson. Med.*, vol. 66, no. 1, pp. 255–263, Jul. 2011.

[11] D. Shrivastava and J. T. Vaughan, “Radiofrequency Heating Models and Measurements,” in *Encyclopedia of Magnetic Resonance*, R. K. Harris, Ed. Chichester, UK: John Wiley & Sons, Ltd, 2011.

[12] European Magnetic Resonance Forum, “Magnetic Resonance, a critical peer-reviewed introduction.” 17-Nov-2014.

[13] D. W. McRobbie, *MRI from picture to proton*. Cambridge, UK; New York: Cambridge University Press, 2003.

[14] H. Zaidi and B. M. W. Tsui, “Review of Computational Anthropomorphic Anatomical and Physiological Models,” *Proc. IEEE*, vol. 97, no. 12, pp. 1938–1953, Dec. 2009.

[15] A. Christ, W. Kainz, E. G. Hahn, K. Honegger, M. Zefferer, E. Neufeld, W. Rascher, R. Janka, W. Bautz, J. Chen, B. Kiefer, P. Schmitt, H.-P. Hollenbach, J. Shen, M. Oberle, D. Szczerba, A. Kam, J. W. Guag, and N. Kuster, “The Virtual Family—development of surface-based anatomical models of two adults and two children for dosimetric simulations,” *Phys. Med. Biol.*, vol. 55, no. 2, pp. N23–N38, Jan. 2010.

[16] “Mimics | Biomedical software and solutions for Engineering on Anatomy.” [Online]. Available: http://biomedical.materialise.com/mimics. [Accessed: 06-Mar-2013].

[17] “SIM4LIFE » zurich med tech.” [Online]. Available: http://www.zurichmedtech.com/sim4life/. [Accessed: 23-Jul-2015].

[18] T. S. Ibrahim, C. Mitchell, R. Abraham, and P. Schmalbrock, “In-depth study of the electromagnetics of ultrahigh-field MRI,” *NMR Biomed.*, vol. 20, no. 1, pp. 58–68, Feb. 2007.

[19] D. Shrivastava, T. Hanson, R. Schlentz, W. Gallaghar, C. Snyder, L. DelaBarre, S. Prakash, P. Iaizzo, and J. T. Vaughan, “Radiofrequency heating at 9.4T: In vivo temperature measurement results in swine,” *Magn. Reson. Med.*, vol. 59, no. 1, pp. 73–78, Jan. 2008.

[20] A. L. H. M. W. van Lier, A. N. T. J. Kotte, B. W. Raaymakers, J. J. W. Lagendijk, and C. A. T. van den Berg, “Radiofrequency heating induced by 7T head MRI: Thermal assessment using discrete vasculature or pennes’ bioheat equation,” *J. Magn. Reson. Imaging*, vol. 35, no. 4, pp. 795–803, Apr. 2012.

[21] C. M. Collins, W. Liu, J. Wang, R. Gruetter, J. T. Vaughan, K. Ugurbil, and M. B. Smith, “Temperature and SAR calculations for a human head within volume and surface coils at 64 and 300 MHz,” *J. Magn. Reson. Imaging*, vol. 19, no. 5, pp. 650–656, May 2004.

[22] M. F. Dempsey and B. Condon, “Thermal Injuries Associated with MRI,” *Clin. Radiol.*, vol. 56, no. 6, pp. 457–465, Jun. 2001.

[23] H. Homann, P. Börnert, H. Eggers, K. Nehrke, O. Dössel, and I. Graesslin, “Toward individualized SAR models and in vivo validation,” *Magn. Reson. Med.*, vol. 66, no. 6, pp. 1767–1776, Dec. 2011.

[24] International Electrotechnical Commission, International Electrotechnical Commission, and Technical Committee 62, *Medical electrical equipment. Appareils électromédicaux. Part 2-33, Partie 2-33, Part 2-33, Partie 2-33,*. Geneva: International Electrotechnical Commission, 2010.

[25] Liang Zhu, “Bioheat Transfer,” in *Standard handbook of biomedical engineering and design*, McGraw-Hill, 2003.

[26] H. H. Pennes, “Analysis of tissue and arterial blood temperatures in the resting human forearm,” *J. Appl. Physiol.*, vol. 1, no. 2, pp. 93–122, 1948.

[27] E. H. Wissler, “Pennes’ 1948 paper revisited,” *J. Appl. Physiol.*, vol. 85, no. 1, pp. 35–41, 1998.

[28] C. K. Charny, S. Weinbaum, and R. L. Levin, “An Evaluation of the Weinbaum-Jiji Bioheat Equation for Normal and Hyperthermic Conditions,” *J. Biomech. Eng.*, vol. 112, no. 1, p. 80, 1990.

[29] S. Weinbaum, L. X. Xu, L. Zhu, and A. Ekpene, “A New Fundamental Bioheat Equation for Muscle Tissue: Part I—Blood Perfusion Term,” *J. Biomech. Eng.*, vol. 119, no. 3, p. 278, 1997.

[30] D. Yang, M. C. Converse, D. M. Mahvi, and J. G. Webster, “Expanding the Bioheat Equation to Include Tissue Internal Water Evaporation During Heating,” *IEEE Trans. Biomed. Eng.*, vol. 54, no. 8, pp. 1382–1388, Aug. 2007.

[31] C. K. Charny, “Mathematical Models of Bioheat Transfer,” in *Advances in Heat Transfer*, vol. 22, Elsevier, 1992, pp. 19–155.

[32] D. Shrivastava and J. T. Vaughan, “A Generic Bioheat Transfer Thermal Model for a Perfused Tissue,” *J. Biomech. Eng.*, vol. 131, no. 7, p. 074506, 2009.

[33] Hasgall PA, Di Gennaro F, Baumgartner C, Neufeld E, Gosselin MC, Payne D, Klingenböck A, Kuster N, "'IT'IS Database for thermal and electromagnetic parameters of biological tissues,.'" .

[34] Allen Taflove and Susan C. Hagness, *Computational Electrodynamics: The Finite-Difference Time-Domain Method.* Boston, MA: Artech House, Inc., 2005.

[35] T. S. Ibrahim, R. Lee, B. A. Baertlein, Y. Yu, and P. M. Robitaille, "Computational analysis of the high pass birdcage resonator: finite difference time domain simulations for high-field MRI," *Magn. Reson. Imaging*, vol. 18, no. 7, pp. 835–843, Sep. 2000.

[36] "FEKO - EM Simulation Software." [Online]. Available: https://www.feko.info/. [Accessed: 11-Aug-2015].

[37] Z. Wang and J. Lin, "SAR Calculations in MRI Scanning Systems [Health Effects]," *IEEE Microw. Mag.*, vol. 13, no. 5, pp. 22–29, Jul. 2012.

[38] C. M. Collins, W. Liu, J. Wang, R. Gruetter, J. T. Vaughan, K. Ugurbil, and M. B. Smith, "Temperature and SAR calculations for a human head within volume and surface coils at 64 and 300 MHz," *J. Magn. Reson. Imaging*, vol. 19, no. 5, pp. 650–656, May 2004.

[39] J. T. Vaughan and J. R. Griffiths, *RF coils for MRI*. Chichester: Wiley, 2012.

[40] C. M. Collins and Z. Wang, "Calculation of radiofrequency electromagnetic fields and their effects in MRI of human subjects," *Magn. Reson. Med.*, vol. 65, no. 5, pp. 1470–1482, May 2011.

[41] P.-M. Robitaille and L. J. Berliner, *Ultra high field magnetic resonance imaging*. New York, NY: Springer, 2006.